



















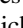


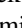

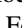
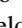
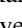



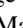
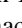





A Systematic Search of Zwicky Transient Facility Data for Ultracompact Binary LISA-detectable Gravitational-wave Sources

Kevin B. Burdge¹ , Thomas A. Prince¹ , Jim Fuller¹ , David L. Kaplan² , Thomas R. Marsh³ ,
Pier-Emmanuel Tremblay³ , Zhuyun Zhuang¹ , Eric C. Bellm⁴ , Ilaria Caiazzo¹ , Michael W. Coughlin⁵ ,
Vik S. Dhillon^{6,7} , Boris Gaensicke³ , Pablo Rodríguez-Gil^{7,8} , Matthew J. Graham¹ , JJ Hermes⁹ , Thomas Kupfer¹⁰ ,
S. P. Littlefair⁶ , Przemek Mróz¹ , E. S. Phinney¹¹ , Jan van Roestel¹ , Yuhan Yao¹ , Richard G. Dekany¹² ,
Andrew J. Drake¹ , Dmitry A. Duev¹ , David Hale¹² , Michael Feeney¹² , George Helou¹³ , Stephen Kaye¹² ,
Ashish. A. Mahabal^{1,14} , Frank J. Masci¹³ , Reed Riddle¹² , Roger Smith¹² , Maayane T. Soumagnac^{15,16} , and
S. R. Kulkarni¹ 

¹ Division of Physics, Mathematics and Astronomy, California Institute of Technology, Pasadena, CA 91125, USA

² Department of Physics, University of Wisconsin-Milwaukee, Milwaukee, WI, USA

³ Department of Physics, University of Warwick, Coventry, CV4 7AL, UK

⁴ DIRAC Institute, Department of Astronomy, University of Washington, 3910 15th Avenue NE, Seattle, WA 98195, USA

⁵ School of Physics and Astronomy, University of Minnesota, Minneapolis, MN 55455, USA

⁶ Department of Physics & Astronomy, University of Sheffield, Sheffield, UK

⁷ Instituto de Astrofísica de Canarias, Vía Láctea s/n, La Laguna, E-38205 Tenerife, Spain

⁸ Departamento de Astrofísica, Universidad de La Laguna, E-38206 La Laguna, Tenerife, Spain

⁹ Department of Astronomy, Boston University, 725 Commonwealth Avenue, Boston, MA 02215, USA

¹⁰ Kavli Institute for Theoretical Physics, University of California, Santa Barbara, CA 93106, USA

¹¹ Theoretical Astrophysics, 350-17 California Institute of Technology, Pasadena CA 91125, USA

¹² Caltech Optical Observatories, California Institute of Technology, Pasadena, CA, USA

¹³ IPAC, California Institute of Technology, 1200 E. California Boulevard, Pasadena, CA 91125, USA

¹⁴ Center for Data Driven Discovery, California Institute of Technology, Pasadena, CA 91125, USA

¹⁵ Lawrence Berkeley National Laboratory, 1 Cyclotron Road, Berkeley, CA 94720, USA

¹⁶ Department of Particle Physics and Astrophysics, Weizmann Institute of Science, Rehovot 76100, Israel

Received 2020 September 4; revised 2020 October 13; accepted 2020 October 15; published 2020 December 9

Abstract

Using photometry collected with the Zwicky Transient Facility, we are conducting an ongoing survey for binary systems with short orbital periods ($P_b < 1$ hr) with the goal of identifying new gravitational-wave sources detectable by the upcoming Laser Interferometer Space Antenna (LISA). We present a sample of 15 binary systems discovered thus far, with orbital periods ranging from 6.91 to 56.35 minutes. Of the 15 systems, seven are eclipsing systems that do not show signs of significant mass transfer. Additionally, we have discovered two AM Canum Venaticorum systems and six systems exhibiting primarily ellipsoidal variations in their lightcurves. We present follow-up spectroscopy and high-speed photometry confirming the nature of these systems, estimates of their LISA signal-to-noise ratios, and a discussion of their physical characteristics.

Unified Astronomy Thesaurus concepts: Compact binary stars (283); Close binary stars (254); Interacting binary stars (801); Eclipsing binary stars (444); Ellipsoidal variable stars (455); Gravitational wave sources (677); White dwarf stars (1799)

1. Introduction

The upcoming Laser Interferometer Space Antenna (LISA; Amaro-Seoane et al. 2017) will be a space-based millihertz-frequency gravitational-wave detector. Astrophysical sources of gravitational radiation in this frequency band include merging supermassive black hole binaries, extreme-mass-ratio inspirals, and Galactic binaries with short orbital periods. With an anticipated number of more than 10,000 detectable sources in the Milky Way (Nissanke et al. 2012), close double-degenerate binaries are by far the largest population of detectable gravitational-wave sources, but only a few have been discovered to date (Kupfer et al. 2018). This population of sources presents a unique opportunity to use the synergy of information carried by electromagnetic and gravitational radiation to understand processes such as binary evolution, the population of Type Ia supernova and R Coronae Borealis (R CrB) progenitors (Webbink 1984), tidal physics in degenerate objects (Fuller & Lai 2012), and Galactic structure (Korol et al. 2019); however, because these sources are so numerous, they will also present a technical

challenge by acting as a formidable background for LISA (Nelemans et al. 2001).

Since the beginning of science operations in 2018 March, the Zwicky Transient Facility (ZTF; Bellm et al. 2019; Graham et al. 2019; Masci et al. 2019; Dekany et al. 2020) has accumulated hundreds of epochs across the northern sky, with more than a thousand in some regions. Here, we present results from a new survey using ZTF data with the goal of discovering LISA sources in the optical time domain. The survey identifies objects that undergo periodic flux variations on short time-scales. We conduct additional spectroscopic and photometric follow-up of objects that exhibit a strong periodic signal with a period shorter than 30 minutes, which also recovers many binaries exhibiting significant power at twice their orbital frequency, such as those dominated by ellipsoidal modulation. By targeting objects in this manner in an all-sky survey, we can search millions of candidates, in contrast to the narrower selection criteria used in surveys such as the highly successful Extremely Low Mass (ELM) survey. The ELM survey

Table 1
ZTF/PTF Short-period Binaries

Name	R.A. (h:m:s)	Decl. (d:m:s)	Orbital Period (minutes)	Nature of Photometric Variability	Spectroscopic Characteristics
ZTF J1539+5027 (1)	15:39:32.16	+50:27:38.72	6.91	Eclipsing+irradiation	DA, double-lined
ZTF J0538+1953	05:38:02.73	+19:53:02.89	14.44	Eclipsing+irradiation	DA, double-lined
ZTF J1905+3134	19:05:11.34	+31:34:32.37	17.20	Eclipsing high state AM CVn	Double-peaked He II emission
PTF J0533+0209 (2)	05:33:32.06	+02:09:11.51	20.57	Ellipsoidal	DBA single-lined
ZTF J2029+1534	20:29:22.31	+15:34:30.97	20.87	Eclipsing	DA, double-lined
ZTF J0722–1839	07:22:21.49	–18:39:30.57	23.70	Eclipsing	DA, double-lined
ZTF J1749+0924	17:49:55.30	+09:24:32.40	26.43	Eclipsing	DA, double-lined
ZTF J2228+4949	22:28:27.07	+49:49:16.44	28.56	High State AM CVn	Double-peaked He II emission
ZTF J1946+3203	19:46:03.89	+32:03:13.13	33.56	Eclipsing+Ellipsoidal	DAB/sdB, single-lined
ZTF J0643+0318	06:43:36.77	+03:18:27.45	36.91	Accreting He star	He I absorption/He II emission
ZTF J0640+1738	06:40:18.69	+17:38:45.01	37.27	Ellipsoidal	sdB, single-lined
ZTF J2130+4420 (3)	21:30:56.71	+44:20:46.42	39.34	Ellipsoidal	sdB, single-lined
ZTF J1901+5309 (4)	19:01:25.42	+53:09:29.27	40.60	Eclipsing	DA, double-lined
ZTF J2320+3750	23:20:20.43	+37:50:30.84	55.25	Ellipsoidal	DA, single-lined
ZTF J2055+4651 (5)	20:55:15.98	+46:51:06.45	56.35	Eclipsing+Ellipsoidal	sdB, single-lined

Note. Coordinates and basic photometric and spectroscopic characteristics of the 15 short-period binaries discovered so far using PTF/ZTF data. Coordinates are taken from Gaia DR2 and are in J2015.0. For apparent magnitudes, see Table 2. More precise orbital periods and uncertainties are reported in Table 3. Please note that in the spectroscopic characteristics column, a DA atmosphere indicates a hydrogen rich white dwarf atmosphere, DBA a helium rich with traces of hydrogen atmosphere, and DAB a hydrogen rich with traces of helium atmosphere.

References. (1) Burdge et al. (2019a), (2) Burdge et al. (2019b), (3) Kupfer et al. (2020b), (4) Coughlin et al. (2019), (5) Kupfer et al. (2020a).

spectroscopically followed up all candidates in a narrow parameter space, resulting in the discovery of 98 detached double-white dwarfs (DWDs), over half of the known double-degenerate population (Brown et al. 2010, 2012, 2013, 2016, 2020b; Kilic et al. 2011, 2012; Gianninas et al. 2015), including several systems that are strong candidate LISA-detectable gravitational-wave sources (Brown et al. 2011, 2020a; Kilic et al. 2014). Until recently, there were only seven known detached binaries with periods less than an hour, two of which were eclipsing, all discoveries made by the ELM survey (Brown et al. 2011, 2017, 2020b).

In 2018 June, using ZTF’s first internal data release, we discovered the shortest-orbital-period eclipsing binary system known, ZTF J1539+5027, with an orbital period of just 6.91 minutes (Burdge et al. 2019a). We originally tested the viability of a photometric selection strategy using archival Palomar Transient Factory (PTF) data (Law et al. 2009), and we discovered PTF J0533+0209, a ≈ 20.6 minute orbital period detached helium-rich DBA WD binary (Burdge et al. 2019b). Since these two discoveries, we have confirmed 13 additional short-period binary systems either spectroscopically via radial velocity shifts or photometrically if they exhibit eclipses (an unambiguous indicator of binarity). These systems are diverse and include detached DWDs, accreting AM Canum Venaticorum (AM CVn) objects (Ramsay et al. 2018), and accreting systems involving helium stars/hot subluminal subdwarfs (sdBs/sdOs; Heber 2016). Even among just the detached DWD population, there exists a rich phase space of possible combinations of core compositions involving helium-core white dwarfs (He WD) and carbon–oxygen-core WDs (CO WD), each of which originate from distinct evolutionary scenarios. Thus, in this work, we devote some discussion to describing the unique characteristics of each system. As a point of reference to guide the reader, we have included Table 1 to highlight essential characteristics of the 15 systems discussed in this work.

2. Methods

2.1. Sample Selection

We used the Pan-STARRS1 (PS1) source catalog (Chambers et al. 2016) to select our sample of objects to period search. Focusing on “blue” objects, we imposed a photometric color selection of $(g - r) < 0.2$ and additionally $(r - i) < 0.2$ (see Table 2). We selected blue objects because we expected that close binary WDs, especially those at orbital periods sufficiently short to be strong LISA sources, should have elevated temperatures due to tidal heating (Fuller & Lai 2013).

2.2. ZTF Photometry

We used ZTF photometry to identify all of our sources (with the exception of PTF J0533+0209). ZTF is a northern-sky synoptic survey based on the 48 inch Samuel Oschin Schmidt telescope at Palomar Observatory, surveying the sky in ZTF g -, r -, and i -bands down to a decl. of -28° with 30 s exposures. ZTF has a 47 deg² field of view and a median 5σ limiting magnitude of 20.8 in g -band, 20.6 in r -band, and 20.2 in i -band. The instrument’s large field of view allows it to rapidly accumulate a large number of epochs across the sky, and the resulting dense sampling serves as a crucial element in identifying sources. All objects in the publication were discovered on or before 2020 March 1. All data from public survey observations were made public in ZTF DR2. All other data is subject to an 18-month proprietary period before it is released to the public.

2.3. Period Finding

Because the fidelity of period finding depends strongly on the number of samples in a lightcurve (especially at short periods where there are large numbers of trial frequencies), rather than impose a cutoff on apparent magnitude, we instead required a minimum of 50 total photometric 5σ detections in

Table 2
Optical and Ultraviolet Apparent Magnitudes of the Sample and Number of ZTF Epochs

Survey: Filter:	GALEX FUV (mag)	GALEX NUV (mag)	Pan-STARRS1 <i>g</i> (mag)	Pan-STARRS1 <i>r</i> (mag)	Pan-STARRS1 <i>i</i> (mag)	Gaia <i>G</i> (mag)	No. of ZTF Epochs <i>r</i> and <i>g</i>
ZTF J1539+5027	18.754 ± 0.084	19.334 ± 0.073	20.134 ± 0.041	20.521 ± 0.069	20.805 ± 0.049	20.491 ± 0.017	1432
ZTF J0538+1953		19.59 ± 0.16	18.777 ± 0.015	18.881 ± 0.011	19.1049 ± 0.0060	18.8346 ± 0.0061	478
ZTF J1905+3134			20.778 ± 0.046	21.15 ± 0.28	21.19 ± 0.13	20.900 ± 0.030	1850
PTF J0533+0209		20.38 ± 0.28	18.995 ± 0.015	19.150 ± 0.013	19.405 ± 0.014	19.1030 ± 0.0075	4795 (PTF)
ZTF J2029+1534	20.12 ± 0.23	20.49 ± 0.20	20.380 ± 0.024	20.662 ± 0.047	20.962 ± 0.093	20.5745 ± 0.0118	690
ZTF J0722−1839			18.976 ± 0.012	19.194 ± 0.016	19.4888 ± 0.0095	19.1040 ± 0.0061	523
ZTF J1749+0924	20.19 ± 0.26		20.357 ± 0.022	20.474 ± 0.014	20.666 ± 0.029	20.538 ± 0.013	1280
ZTF J2228+4949		19.43 ± 0.12	19.317 ± 0.028	19.390 ± 0.034	19.571 ± 0.022	19.2758 ± 0.0060	3082
ZTF J1946+3203			19.400 ± 0.035	19.266 ± 0.020	19.240 ± 0.025	19.1905 ± 0.0059	1270
ZTF J0643+0318		21.68 ± 0.48	18.384 ± 0.012	18.269 ± 0.058	18.306 ± 0.037	18.271 ± 0.019	510
ZTF J0640+1738			19.222 ± 0.017	19.409 ± 0.024	19.486 ± 0.016	19.2521 ± 0.0062	842
ZTF J2130+4420		15.727 ± 0.012	15.3269 ± 0.0049	15.6412 ± 0.0078	15.806 ± 0.028	15.4611 ± 0.0061	2334
ZTF J1901+5309		17.331 ± 0.041	17.8909 ± 0.0055	18.2512 ± 0.0031	18.5764 ± 0.0055	18.0686 ± 0.0023	4254
ZTF J2320+3750		21.39 ± 0.28	19.411 ± 0.024	19.394 ± 0.025	19.536 ± 0.028	19.3997 ± 0.0070	992
ZTF J2055+4651			17.720 ± 0.042	17.652 ± 0.023	17.647 ± 0.015	17.6539 ± 0.0093	1820

Note. The Pan-STARRS1 and GALEX apparent magnitudes are given in the AB system, while Gaia magnitudes are given in the Vega system.

archival ZTF data. This selection produced approximately 10 million candidates to search, and we estimate that this sample should include $>90\%$ of objects in the Pan-STARRS color cut above a decl. of -28° with $G > 19.0$ m in Gaia, with the completeness falling off significantly at fainter apparent magnitudes due to blending in the Galactic plane; the appendix provides further details on this estimate. We combined data from multiple filters by computing the median magnitude in each filter and shifting the g -band and i -band so that their median magnitudes matched the r -band data. We do this in order to maximize the number of epochs available in each lightcurve. We used a graphics processing unit implementation of the conditional entropy period-finding algorithm (Graham et al. 2013) and later the Box Least Squares (BLS) algorithm (Kovács et al. 2002). Although BLS is optimized for identifying eclipsing systems, conditional entropy is computationally less costly and was responsible for the discovery of 12 of the 15 systems in the sample. The only system discovered in a later BLS search was ZTF J1749+0924. We originally discovered ZTF J2130+4420, which is the brightest object in the sample, using the analysis-of-variance (AOV) algorithm (Schwarzenberg-Czerny 1996) in a search of bright sources between the WD track and the main sequence. It was later recovered by both the conditional entropy algorithm and as part of a search of the hot subdwarf catalog (Geier et al. 2017) as discussed in Kupfer et al. (2020b; PTF J0533+0209 was also discovered with the AOV algorithm; see Burdge et al. 2019b). The BLS algorithm is able to recover all systems as well, but with greater than an order of magnitude longer run time relative to conditional entropy. The conditional entropy algorithm phase-folds lightcurves on a grid of trial frequencies, partitions the lightcurve into magnitude and phase bins, and computes the conditional entropy of the partitioned, phase-folded lightcurve corresponding to each frequency. For further details on the sensitivity of this algorithm, please see the appendix. We wish to note that this work does not explore the recovery efficiency of the period-finding method used in great detail, though a superficial discussion is included in the appendix. When we explored this topic, we discovered it is quite nuanced for a number of reasons, including the effects of catastrophic photometric outliers, blending in crowded regions of the Galactic plane, and the nature of the ZTF archive, which only records 5σ detections without preserving information regarding nondetections, meaning that when variable sources are near ZTF’s detection threshold, the lowest flux measurements are systematically omitted (which wreaks havoc on the fidelity of period finding, especially for eclipsing systems where most of the information content lies in these points). In order to robustly understand detection efficiency, dedicated work is underway to simulate realistic ZTF lightcurves of synthetic data. An additional complication in estimating recovery as a function of sky position is that ZTF’s proprietary surveys have a highly inhomogeneous cadence, meaning that recovery efficiency depends on sky location in a complex manner. In general, the sample of objects we discovered were found at low Galactic latitudes, with eight of the 15 systems falling at $|b| < 10^\circ$, and only two of the systems with $|b| > 20^\circ$.

We determine the best period of the object by selecting the trial frequency that minimizes the conditional entropy. We visually inspect the most significant phase-folded lightcurves (all with significance greater than 8), where significance is simply defined as the minimum entropy value divided by the

standard deviation of entropy values across the full periodogram, and from this we select the most promising candidates for follow-up. We performed this visual inspection on 24,635 lightcurves with a minimum entropy corresponding to a period below 30 minutes, and we determined that 337 of these were likely real periodic signals based on the appearance of their lightcurves. We then began to systematically follow up on systems that exhibited photometric behavior suggestive of binarity (eclipses or asymmetric minima in ellipsoidal variables). Follow-up of objects in this sample is ongoing.

One challenge of searching for periodic variables in a sample of millions of objects over a large frequency grid (for further details see the appendix) is the increase in opportunity for objects to exhibit significant random fluctuations in their power spectra. This means that many of the lower-amplitude periodic variables recovered actually show a smaller “significance” than some nonperiodic objects, hence the value in visually inspecting a moderate number of objects at low significance, rather than only the most significant sources. Note that targeting objects with “best” periods under 30 minutes yielded many discoveries with orbital periods between 30 and 60 minutes, as systems that exhibit ellipsoidal variations and eclipsing systems in which there is a prominent secondary eclipse exhibit significant power at twice their orbital frequency.

The ZTF phase-folded lightcurves of all short-period binary systems discovered from this sample are illustrated in Figure 1.

In order to determine the uncertainties in the orbital period reported in Table 3, we used a jackknifing technique in which we subsampled each ZTF lightcurve 1000 times, using 90% of the points in each subsample, with replacement, and computed the standard deviation of the best periods of the 1000 trials. For ellipsoidal systems, we used Lomb–Scargle (Lomb 1976; Scargle 1982) for this bootstrapping exercise, and for eclipsing systems, we used BLS. For ZTF J1539+5027 and PTF J0533+0209, which have well-measured orbital evolution, we instead used the linear component of the quadratic fit to the timing residuals to determine the uncertainty in the period (for further details, see Burdge et al. 2019a).

Of the short-period candidates recovered by conditional entropy, we immediately identified two as ellipsoidal variables with periods between 30 and 60 minutes (ZTF J2130+4420 and ZTF J2055+4651) because they clearly exhibited significant power at twice their orbital frequency, distinguishing them from the large number of δ Scuti stars in this period range (Breger 2000). Spectroscopic characterization later revealed additional ellipsoidal variables with orbital periods between 30 and 60 minutes. Some candidates exhibiting a dominant period below 30 minutes failed to show indications of binarity in follow-up characterization. Some of these were identified as likely belonging to other classes of short-period variables, including pulsating WDs such as GW Vir, V777 Her, and ZZ Ceti stars (Fontaine & Brassard 2008); hot subdwarf p-mode pulsators (Charpinet et al. 1996); blue large-amplitude pulsators (Pietrukowicz et al. 2017); He WD radial-mode pulsators (Kupfer et al. 2019); and rapidly rotating magnetic WDs (Brinkworth et al. 2013; Reding et al. 2020). One significant source of interlopers in the sample originates from intermediate polars (Patterson 1994), which contain magnetic WDs that have been spun up to a short spin period and exhibit periodicity on the timescale of minutes. These objects often have a blue color, emit X-rays, and can show strong photometric periodicity on minute timescales, due to flux variations in the WD spin period (Ramsay et al. 2008). The

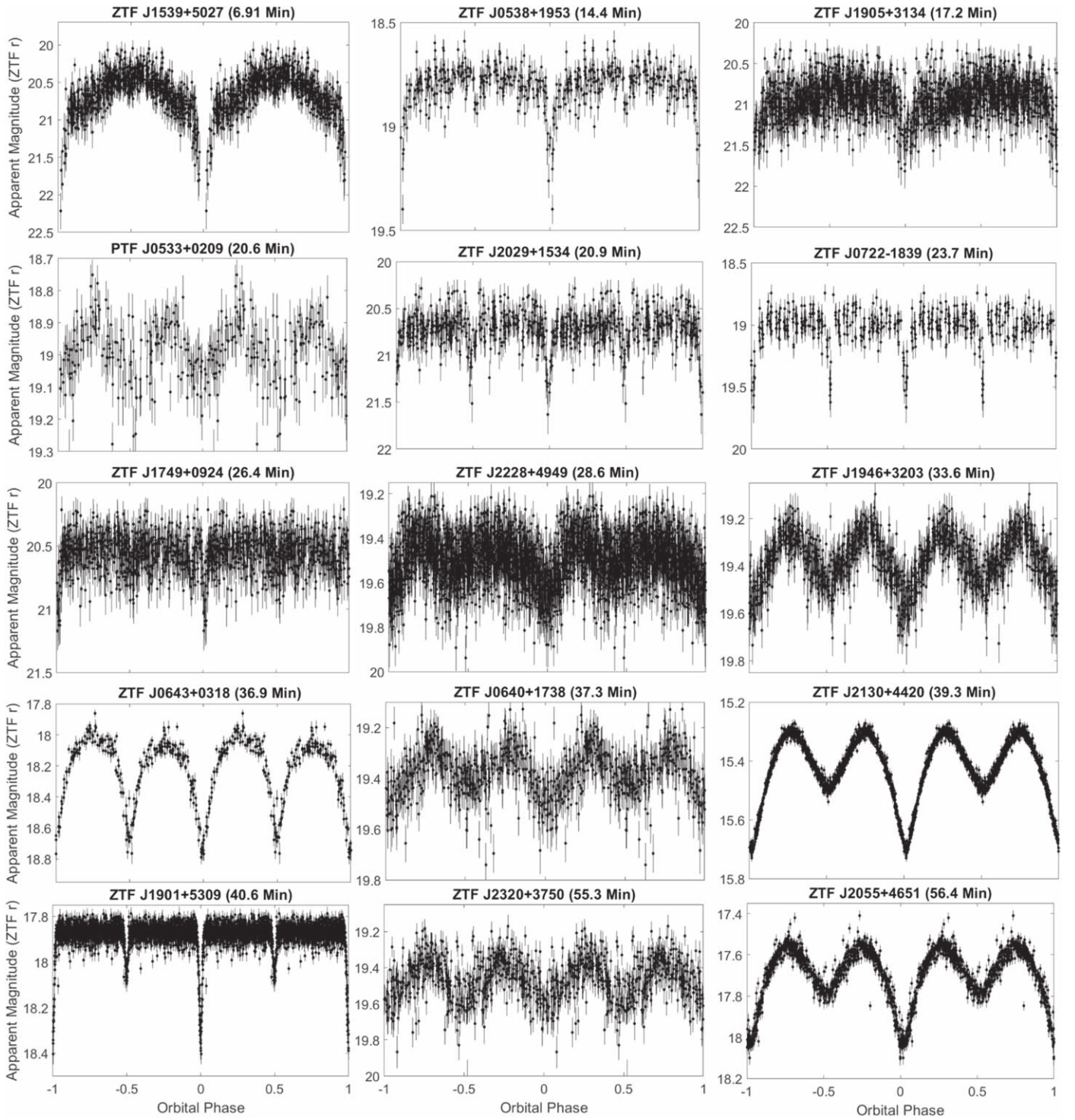


Figure 1. Phase-folded ZTF lightcurves of the sample (all filters combined), at periods as recovered by the algorithm described in Section 2.3.

crucial diagnostic we use to rule out a minute-timescale orbital period in these systems is phase-resolved spectroscopy, as they do not exhibit radial velocity shifts in the WD spin period.

2.4. High-speed Photometry

High-speed photometric follow-up proved a crucial element in characterizing candidates from our period searches, as such observations can confirm the presence of eclipses and more subtle photometric effects such as Doppler beaming and gravity

darkening. In this work, we present data collected from four different high-speed photometers: the Caltech High-speed Multi-color camera (CHIMERA) on the 5.1 m Hale telescope at Palomar observatory (Harding et al. 2016), the Kitt Peak Electron Multiplying CCD Demonstrator (KPED) on the 2.1 m telescope at Kitt Peak National observatory (Coughlin et al. 2019), HiPERCAM on the 10.4 m Gran Telescopio Canarias (Dhillon et al. 2018; V. Dhillon et al. 2020 in preparation), and ULTRACAM on the 3.5 m New Technology Telescope at La Silla observatory (Dhillon et al. 2007). In all cases, the

Table 3
Orbital Characteristics

Quantity:	K_A (km s ⁻¹)	K_B (km s ⁻¹)	i (deg)	T_0 (MBJD _{TDB})	P_b (s)
ZTF J1539+5027 (1)	292 ⁺²⁵⁴ ₋₅₈₃	961 ⁺¹⁷⁸ ₋₁₃₉	84.15 ^{+0.64} _{-0.57}	58305.1827886(12)	414.7915404(29)
ZTF J0538+1953			85.43 ^{+0.07} _{-0.09}	58734.23560684(49)	866.60331(16)
ZTF J1905+3134					1032.16441(62)
PTF J0533+0209 (2)		618.7 ^{+6.9} _{-6.9}	72.8 ^{+0.8} _{-1.4}	58144.596848(46)	1233.9729(17)
ZTF J2029+1534			86.64 ^{+0.70} _{-0.4}	58757.255378(55)	1252.056499(41)
ZTF J0722-1839			89.66 ^{+0.22} _{-0.22}	58874.1823868(11)	1422.548655(71)
ZTF J1749+0924			85.45 ^{+1.40} _{-1.15}	58634.41086(2)	1586.03389(44)
ZTF J2228+4949					1713.58282(25)
ZTF J1946+3203		284.8 ^{+4.8} _{-4.8}	77.08 ^{+1.6} _{-1.2}	58836.38825(13)	2013.82141(75)
ZTF J0643+0318		432.5 ^{+12.0} _{-12.0}			2214.8058(11)
ZTF J0640+1738		315.9 ^{+8.0} _{-8.0}	65.3 ^{+5.1} _{-5.1}	58836.38825(13)	2236.0160(16)
ZTF J2130+4420 (3)		418.5 ^{+2.5} _{-2.5}	86.4 ^{+1.0} _{-1.0}	58672.1808578(1)	2360.4062(14)
ZTF J1901+5309			87.28 ^{+0.52} _{-0.50}	58703.3738042(31)	2436.10817(93)
ZTF J2320+3750		466.0 ^{+9.0} _{-9.0}	84.5 ^{+2.7} _{-3.2}	58769.28488(28)	3314.7998(35)
ZTF J2055+4651 (4)		404.0 ^{+11.0} _{-11.0}	83.3 ^{+0.5} _{-0.5}	58731.944425(1)	3380.8701(29)

Note. Measured orbital parameters for all of our systems, including the radial velocity semiamplitudes of the components, K_A and K_B , the orbital inclination, i , the time of superior conjunction, T_0 , and the orbital period, P_b . All quantities were determined using the analyses described in Section 3, with the exception of ZTF J1539+5027, ZTF J0533+0209, ZTF J2130+4420, and ZTF J2055+4651, whose parameters were taken from previous publications.

References. (1) Burdge et al. (2019a), (2) Burdge et al. (2019b), (3) Kupfer et al. (2020b), (4) Kupfer et al. (2020a).

instruments were run in frame-transfer mode, effectively eliminating readout time overheads. We reduced the CHIMERA, KPED, HiPERCAM, and ULTRACAM data with publicly available pipelines.^{17,18,19} Lightcurves obtained with these instruments are illustrated in Figure 2. For further details on these observations, please see the appendix.

2.5. Spectroscopic Follow-up

We conducted most of our spectroscopy using the Low Resolution Imaging Spectrometer (LRIS; Oke et al. 1995) on the 10 m W.M. Keck I Telescope on Maunakea. Exposure times varied from object to object, but were restricted to be no more than one-eighth of the orbital period in order to minimize Doppler smearing. We reduced all data with the “pipe” pipeline (Perley 2019). For all sequences of exposures, we took a HeNeArCdZn arc at the telescope position of the object at the completion of the sequence in order to ensure stable wavelength calibration (which can depend strongly on instrument flexure). For any sequences of observations exceeding one hour, we obtained an arc at the start and finish of observations, or if longer than two hours, an arc once every two hours. For further details on instrument configuration and other spectrographs used, please see the appendix. The spectra we obtained are presented in Figure 3.

3. Analysis and Results

3.1. Lightcurve Modeling

We used the LCURVE code (Copperwheat et al. 2010) to model and infer physical parameters from the lightcurves we obtained with high-speed photometers. For lightcurves with multiple bands, we simultaneously modeled all bands (measuring the relative surface brightnesses of objects at multiple wavelengths aids in determining the relative temperatures of

the objects in the system). For all objects, we used the following set of free parameters: the mass ratio $q = \frac{M_B}{M_A}$, the inclination i , the radius of the primary component, R_A , the radius of the secondary component, R_B , the temperature of the secondary component, T_B , the mideclipse time, t_0 , and an absorption coefficient α to account for effects in which the cooler component in the binary is irradiated and reprocesses flux originating from the hotter component. We fit for a different α for each band, as radiation reprocessing is wavelength dependent. Measuring the mass ratio, q , from lightcurve modeling arises primarily from fitting ellipsoidal modulation that is due to the tidal deformation of one or both components in the system. The fractional amplitude of ellipsoidal modulation, $\frac{\Delta F_{\text{ellipsoidal}}}{F}$, is given by

$$\frac{\Delta F_{\text{ellipsoidal}}}{F} = 0.15 \frac{(15 + u)(1 + \tau)}{3 - u} \left(\frac{R}{a}\right)^3 q \sin^2(i) \quad (1)$$

(Morris 1985), where u is the passband-dependent linear limb-darkening coefficient, and τ is the passband-dependent gravity-darkening coefficient. We obtain all gravity- and limb-darkening coefficients from Claret et al. (2020a) and Doppler beaming coefficients from Claret et al. (2020b). For our full modeling, we use the four-parameter Claret limb-darkening law described in Claret (2000). Previous work such as that presented in Bloemen et al. (2012) found tension between the mass ratio inferred from purely ellipsoidal modulation and that determined by other less model-dependent measurements such as radial velocity semiamplitudes, which they attributed to the possibility that some close binaries may not be entirely synchronized. At these short orbital periods, we expect some of our systems to be synchronized, but those at longer periods may not be (Fuller & Lai 2012). In any case, we emphasize that mass ratios derived from ellipsoidal modulation come from model-dependent expressions, and thus there is value in obtaining more model-independent measurements in the form

¹⁷ <https://github.com/mcoughlin/kp84>

¹⁸ <https://github.com/HiPERCAM>

¹⁹ <https://github.com/trmrsh/cpp-ultracam>

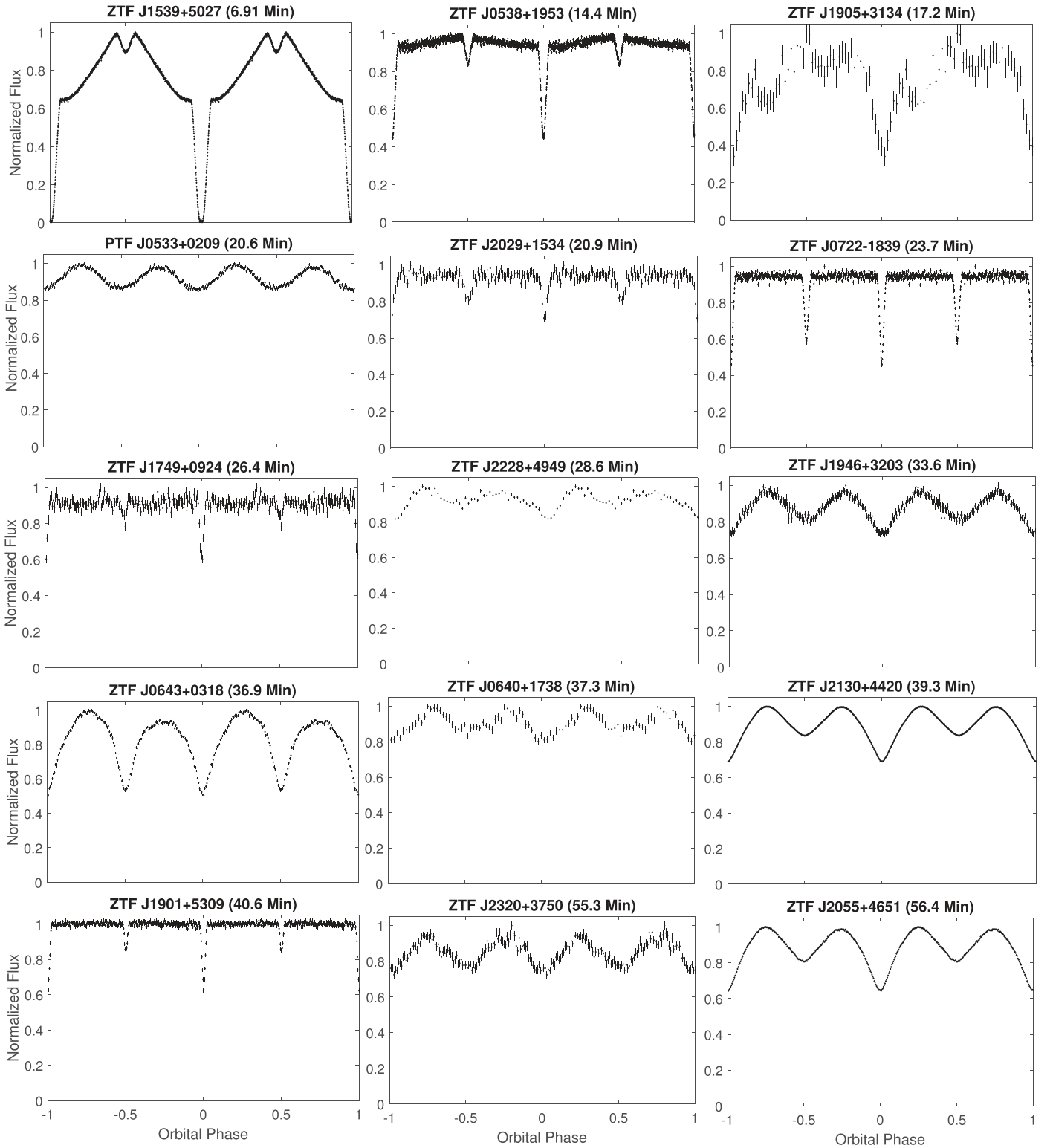


Figure 2. The best available lightcurves for our sample, phase-binned at the orbital periods. See Table 7 for further details on which instruments were used to obtain each lightcurve. J2228+4949 and J0640+1738 have only ZTF lightcurves, so we plot the binned versions of those here. All of these systems were confirmed as binaries via spectroscopic follow-up.

of radial velocity semi-amplitudes as well as orbital decay, due to general relativity (Burdge et al. 2019a).

We estimated masses for five of the eclipsing systems (ZTF J0538+1953, ZTF J2029+1534, ZTF J0722-1839, ZTF J1749+0924, and ZTF J1901+5309) using temperatures derived from

spectroscopy and radii derived from lightcurve modeling. As discussed above, lightcurve modeling allows us to infer the radii of the two component objects with respect to the semimajor axis in these systems. We combined these measurements (as well as our spectroscopic temperature constraints) with the

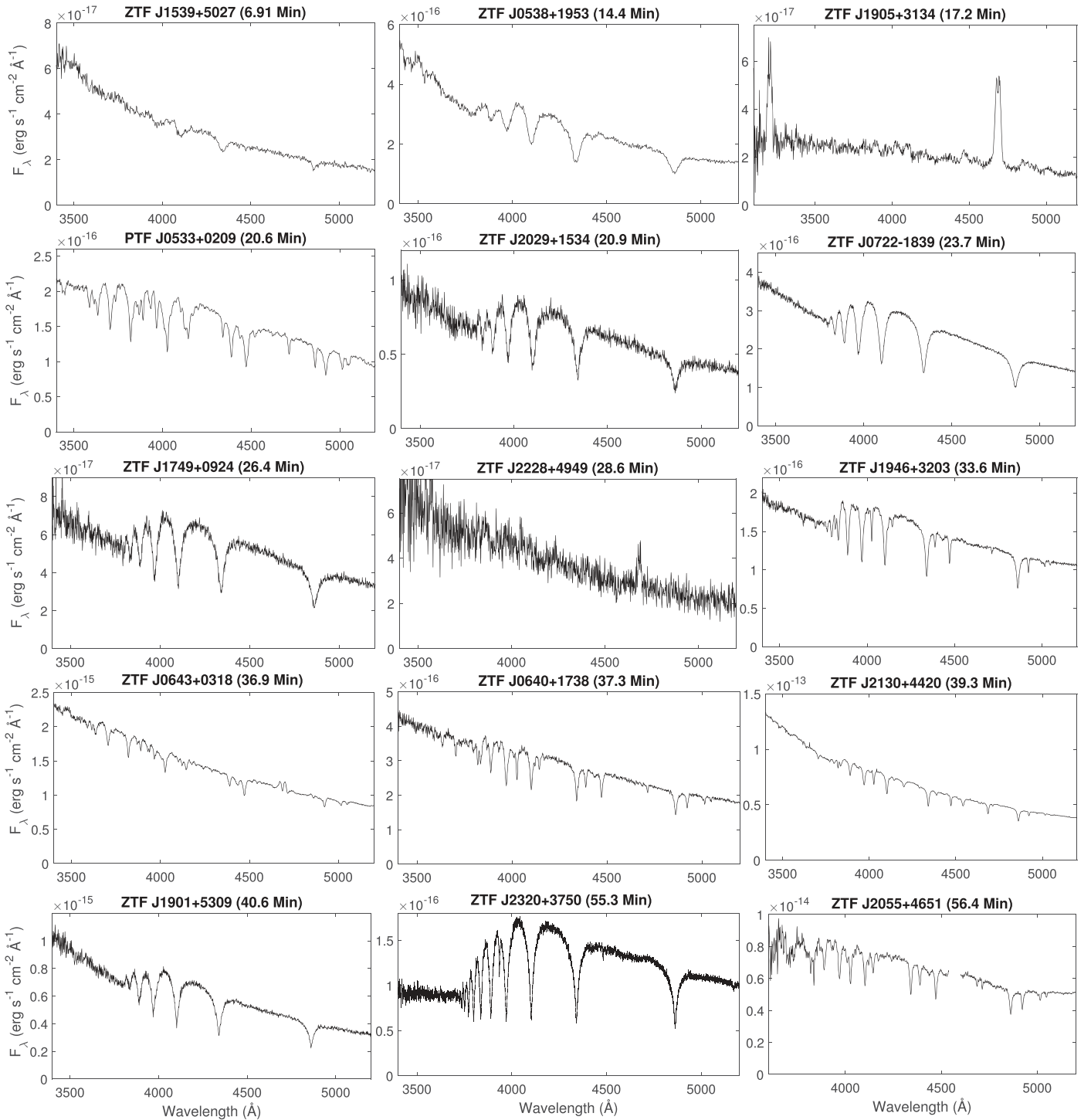


Figure 3. The best-available spectra for our sample, coadded in the rest frame of absorption lines. By fitting these spectra, we were able to obtain radial velocity semiamplitudes for seven systems (see Figure 4) and fit objects for an effective temperature and surface gravity using spectroscopic WD models. We used these spectroscopically derived parameters in combination with lightcurve modeling to derive the physical parameters reported in Table 5. See the appendix for further details on which instruments were used to obtain each spectrum. ZTF J1539+5027, J0538+1953, J2029+1534, J0722–1839, J1749+0924, J1901+5309, and J2320+3750 show hydrogen-rich atmospheres, while J0533+0209, J1946+3203, J0640+1738, J2130+4420, and J2055+4651 exhibit mixed H/He atmospheres, and the three mass-transferring systems, J1905+3134, J2228+4949, and J0643+0318, have only helium lines in their spectra.

semiempirical mass–radius relations described in Soares (2017) in order to estimate the masses of both components. We adopted a 10% model error in estimating our uncertainties based on the scatter of measured radii versus estimated radii reported in Soares (2017), because mass–radius relations (especially for low-mass He WDs) are sensitive to additional degrees of

freedom, such as the mass of the hydrogen envelope on the surface of the WD and the evolutionary history of the object (in particular, the occurrence of hydrogen shell flashes; Istrate et al. 2016). In the future, as we measure orbital decay rates for these systems, we will be able to constrain masses in a more model-independent manner.

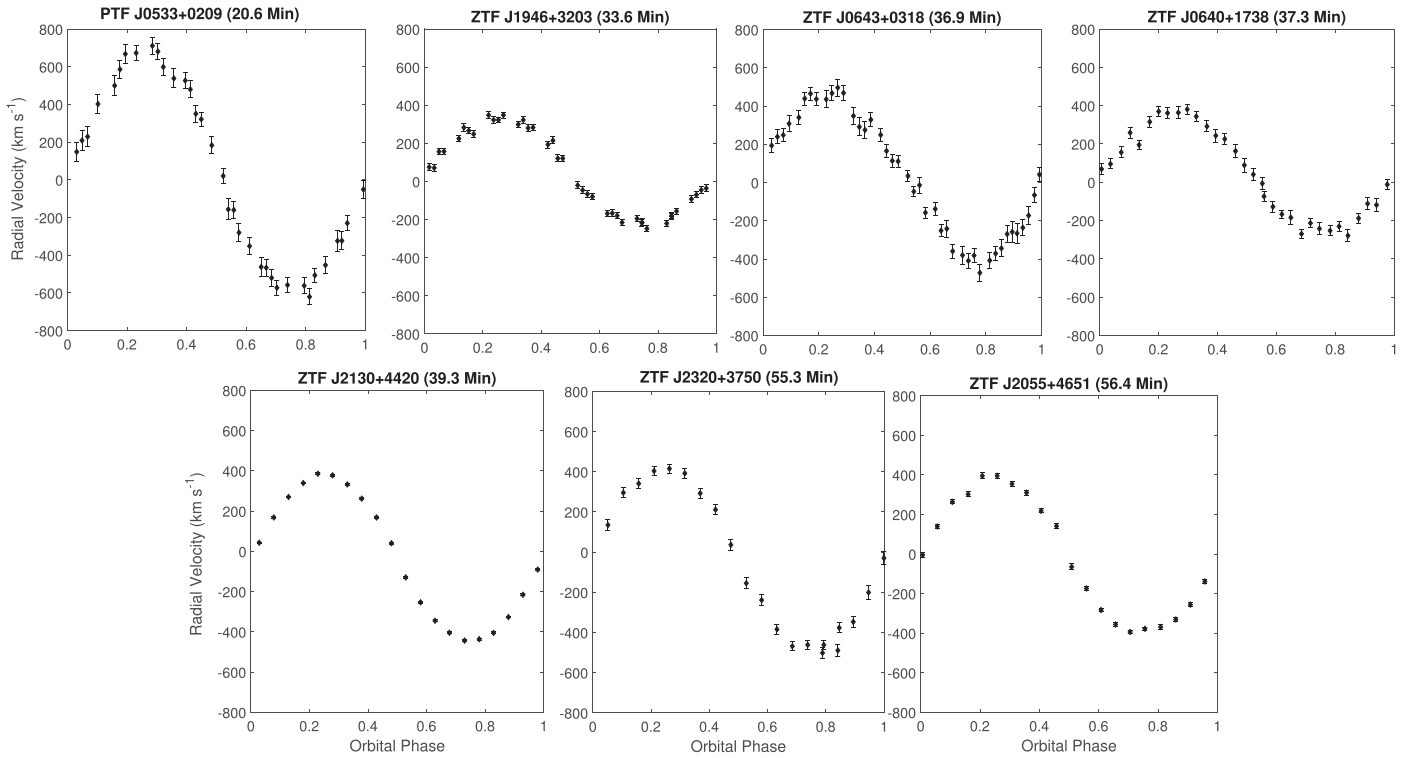


Figure 4. Phase-folded radial velocity measurements for a subset of the sample that is single-lined. All measurements shown are phase-folded according to the orbital period and ephemeris obtained from lightcurve modeling.

3.2. Orbital Dynamics

We acquired phase-resolved spectra for all objects in the sample; however, at this time, we were only able to extract reliable radial velocity solutions for the single-lined systems. For these systems, we measured velocities by fitting Voigt profiles to the Balmer series of absorption lines and to helium absorption lines, when present. Single-lined spectroscopic binaries show a radial velocity from only one of their two components, whereas double-lined systems contain contributions from both. Double-lined systems are in principle more valuable, as one can precisely constrain the mass ratio of the system and, if combined with an inclination constraint from lightcurve modeling, solve for both of the dynamical masses in the system using the binary mass functions

$$\frac{M_A^3 \sin^3(i)}{(M_A + M_B)^2} = \frac{P_b K_B^3}{2\pi G} \quad (2)$$

and

$$\frac{M_B^3 \sin^3(i)}{(M_B + M_A)^2} = \frac{P_b K_A^3}{2\pi G}, \quad (3)$$

where K_A and K_B are the radial velocity semi-amplitudes of the two components, i is the inclination of the system, and P_b is the orbital period. These expressions arise from Newtonian mechanics, so the physics involved is straightforward, allowing for a more robust estimate of masses than those that invoke more complicated physical models, such as WD mass–radius relations, evolutionary tracks, and atmospheric models. However, in practice, fitting double-lined WDs is challenging when the components are both faint and in a short-orbital-period binary. One reason is that the absorption lines in WDs are

intrinsically broad, such that their overlap is significant even at maximum radial velocity shift (they can be several hundred Å across, whereas the Doppler shifts correspond to on the order of 10 Å). WDs do have nonlocal thermodynamic equilibrium (NLTE) cores in their hydrogen absorption lines (Koester et al. 1998) with a narrower FWHM allowing for more precise radial velocity measurements; however, resolving these line cores requires moderate-resolution spectra at good signal-to-noise ratio (S/N). In binary systems with short orbital periods, exposures must be short to avoid significant orbital smearing, and this results in too-few photons per exposure to reliably use medium-resolution spectra without suffering from readout noise. Because of these technical challenges, the work to measure the dynamical masses of the double-lined systems of our sample (e.g., ZTF J0722–1839) is ongoing. See Figure 4 for an illustration of well-measured radial velocities in our sample (for the single-lined systems) and Table 3 for the measured radial velocity semi-amplitudes of objects.

3.3. Spectroscopic Modeling

In addition to being used to measure radial velocities, spectra can be used to estimate the temperature, surface gravity, and atmospheric abundances of stars. For single-lined systems, we fit atmospheric models to the entire spectrum in order to estimate the temperature of the dominant component and supply this temperature to our lightcurve modeling. We perform an iterative process for double-lined systems, due to the spectra being a blend of two WDs (one must account for this because cooler companion WDs can have deeper absorption lines, and thus, even if they contribute only a small fraction of the overall luminosity, they can significantly impact

line profiles). First, we fit a single WD model to the spectrum to estimate the temperature of the dominant component. We then proceed to model the lightcurve while fixing the temperature of the hotter component to this value. Using this model, we can estimate both a surface brightness ratio and a ratio of component radii. We use this information to construct a composite model of two WD atmospheres, and we fit this composite model to the spectra to arrive at the final temperature estimates. For the hydrogen-rich atmosphere DA WD systems, we use the NLTE DA models described in Tremblay et al. (2011) with Stark broadening from Tremblay & Bergeron (2009). For the coolest and lowest surface gravity DA in our sample, ZTF J2320+3750, we use models described in Gianninas et al. (2014) and Tremblay et al. (2015). For modeling lower surface gravity ($\log(g)$) mixed H/He atmosphere objects that could be either hot subdwarfs or young He WDs, we used the model spectra described in Stroeger et al. (2007). Please note that when we refer to He WDs throughout this publication, it indicates helium core composition, not atmospheric composition. We did not factor spectroscopically measured surface gravity into our final parameter estimation, except for in the case of ZTF J2320+3750, in which the He WD component was poorly constrained by mass–radius relations alone because of the significant temperature sensitivity of these relations at such low mass.

3.4. Orbital Evolution

The orbital evolution of short-orbital-period binary systems is dominated by energy loss that is due to the emission of gravitational radiation, but it can also be strongly influenced by the presence of mass transfer in accreting systems, especially ones with large mass ratios such as AM CVns (Postnov & Yungelson 2014). Measuring orbital evolution in detached systems is particularly valuable, as general relativity predicts that the orbital frequency derivative, \dot{f}_{GW} , is directly related to the gravitational-wave frequency $f_{\text{GW}} = \frac{2}{P_b}$ and the chirp mass

of the system, $\mathcal{M} = \frac{(M_A M_B)^{3/5}}{(M_A + M_B)^{1/5}}$, as given by

$$\dot{f}_{\text{GW}} = \frac{96}{5} \pi^{8/3} \left(\frac{G\mathcal{M}}{c^3} \right)^{5/3} f_{\text{GW}}^{11/3} \quad (4)$$

(Taylor & Weisberg 1989).

Conveniently, the strain of gravitational radiation emitted from such a binary depends only on the orbital frequency, chirp mass, and distance to the object, and thus the gravitational-wave strain that LISA will measure is given by

$$S = \frac{2(G\mathcal{M})^{5/3} (\pi f_{\text{GW}})^{2/3}}{c^4 D}, \quad (5)$$

where D is the distance to the system. Multiplying this quantity by $\sqrt{f_{\text{GW}} T_{\text{obs}}}$ gives the characteristic strain, where T_{obs} is the total time LISA has operated (Thorne 1987; Moore et al. 2015). For the characteristic strains computed in this work, T_{obs} is taken to be 4 yr.

By constraining the chirp mass and orbital frequency from optical data, a LISA gravitational-wave signal can be used to infer a distance to the system, which will be particularly useful because most of the objects being discovered are too faint for reliable Gaia astrometric solutions. For overconstrained systems where the distance is well determined via a measurement like the parallax, the gravitational-wave strain could be

compared with that predicted based on an orbital decay rate that is due to purely general relativity, to estimate a deviation in the decay rate from tidal dissipation (Benacquista 2011; Piro 2011). Thus far, orbital decay has been detected and reported for two objects in the sample: ZTF J1539+5027 (Burdge et al. 2019a) and PTF J0533+0209 (Burdge et al. 2019b). The precisely measured decay rates in these two systems were enabled by regular photometric monitoring combined with well-sampled archival Palomar Transient Factory data collected a decade ago. We have not reached this threshold for any other systems, but we continue to monitor all systems for orbital frequency evolution. The uncertainties of the ephemerides reported in Table 3 give a characteristic estimate of the precision with which each system can be timed, and this can be compared to the predicted phase shift in timing residuals given the expected decay rate of the system (see Burdge et al. 2019a for more details) in order to estimate how long it will take to measure the orbital evolution precisely. The period derivative should be easily detectable in all systems before LISA begins to operate if their orbital evolution is dominated by the emission of gravitational waves.

3.5. Distance Estimates

We report our estimated distances to the systems in Table 4. Estimating the distances to systems in our sample is an important element in this work as they are crucial in computing accurate gravitational-wave amplitudes for the sources as measured from the solar system. Most of the systems in our sample have temperature estimates as well as radius estimates; this allows us to compute distances directly based on these values and synthetic spectra for WDs. We use system parameters inferred from a combination of lightcurve modeling and spectroscopic fitting to generate a composite synthetic spectrum for each system, and we compute a synthetic apparent magnitude from these spectra. We chose to compute Pan-STARRS1 g -band apparent magnitudes and compare to the measured value. We use Pan-STARRS1 g due to its availability for all objects and its short wavelength compared to other available passbands, ensuring minimal potential contamination from blended background sources in dense fields (which on average are likely to contribute more to redder bands). These spectroscopic distance estimates are used in computing the LISA S/N. We estimate uncertainties on these distance estimates by setting up a Monte Carlo simulation in which we sample over distance and the temperatures and radii of both WDs (with priors set by the lightcurve+spectroscopic analysis). During each iteration, we use the two temperatures and radii to generate a synthetic spectrum, and we automatically query the reddening catalog described in Green et al. (2019) at the coordinates of the source using the distance sample from that iteration to estimate the reddening along the line of sight. We use this to apply a reddening correction to the synthetic photometry we generate. We then compare this synthetic flux to the measured Pan-STARRS1 g and compute the likelihood function using the uncertainty reported by Pan-STARRS1. The spectroscopic distances reported in Table 4 were computed using the posterior distribution of this analysis.

It is worth noting that Gaia has revolutionized astronomy by providing the capability to estimate distances to a large number of stars in the Galaxy via the measurement of parallax. However, for faint populations of sources with uncertain parallaxes, there are subtleties to inferring distance from the

Table 4
Distance and Reddening Estimates

Technique:	Spectroscopic (kpc)	Bailer-Jones (kpc)	400 pc Length Scale (kpc)	$E(g-r)$ (m_{AB})	Gaia $\bar{\omega}$ (mas)	Gaia μ R.A. (mas yr $^{-1}$)	Gaia μ Decl. (mas yr $^{-1}$)
ZTF J1539+5027	$2.34^{+0.14}_{-0.14}$	$1.39^{+0.87}_{-0.53}$	$1.25^{+0.72}_{-0.45}$		-0.11 ± 0.79	-3.41 ± 1.53	-3.82 ± 1.58
ZTF J0538+1953	$0.684^{+0.018}_{-0.014}$	$1.07^{+1.48}_{-0.45}$	$0.84^{+0.46}_{-0.26}$	$0.25^{+0.02}_{-0.02}$	1.15 ± 0.48	-2.22 ± 0.54	-5.67 ± 0.45
ZTF J1905+3134	3.8–9.5						
PTF J0533+0209	$1.74^{+0.14}_{-0.14}$	$1.54^{+1.06}_{-0.58}$	$1.23^{+0.63}_{-0.40}$	$0.11^{+0.02}_{-0.02}$	0.47 ± 0.48	1.43 ± 0.74	2.56 ± 0.91
ZTF J2029+1534	$2.02^{+0.15}_{-0.15}$	$2.39^{+1.89}_{-1.17}$	$1.17^{+0.74}_{-0.47}$	$0.08^{+0.03}_{-0.01}$	-1.43 ± 1.43	-5.94 ± 1.51	-9.92 ± 1.93
ZTF J0722–1839	$0.928^{+0.023}_{-0.031}$	$2.51^{+2.28}_{-1.10}$	$1.41^{+0.61}_{-0.42}$	$0.14^{+0.03}_{-0.01}$	0.41 ± 0.35	-5.83 ± 0.52	4.18 ± 0.65
ZTF J1749+0924	$1.55^{+0.20}_{-0.18}$	$3.34^{+2.55}_{-1.58}$	$1.34^{+0.76}_{-0.50}$	$0.13^{+0.03}_{-0.01}$	-2.68 ± 1.36	-6.50 ± 2.78	6.90 ± 3.74
ZTF J2228+4949	0.72–1.77	$1.79^{+1.48}_{-0.67}$	$1.31^{+0.54}_{-0.36}$	$0.14^{+0.02}_{-0.02}$	0.57 ± 0.31	-3.83 ± 0.56	-2.56 ± 0.53
ZTF J1946+3203	$2.38^{+0.18}_{-0.20}$	$2.18^{+4.12}_{-1.08}$	$1.15^{+0.51}_{-0.33}$	$0.14^{+0.02}_{-0.04}$	0.72 ± 0.35	-1.86 ± 0.46	-4.27 ± 0.49
ZTF J0643+0318		$2.13^{+1.59}_{-0.74}$	$1.55^{+0.51}_{-0.39}$	$0.45^{+0.02}_{-0.05}$	0.47 ± 0.22	0.71 ± 0.40	1.50 ± 0.41
ZTF J0640+1738	$5.9^{+1.3}_{-1.2}$	$1.90^{+1.61}_{-0.80}$	$1.24^{+0.61}_{-0.39}$	$0.12^{+0.02}_{-0.02}$	0.51 ± 0.44	-0.36 ± 1.16	1.10 ± 1.33
ZTF J2130+4420	$1.209^{+0.046}_{-0.047}$	$1.116^{+0.043}_{-0.040}$	$1.16^{+0.10}_{-0.08}$	$0.18^{+0.02}_{-0.02}$	0.833 ± 0.031	0.009 ± 0.031	-1.682 ± 0.0048
ZTF J1901+5309	$0.831^{+0.050}_{-0.047}$	$0.89^{+0.11}_{-0.09}$	$0.88^{+0.08}_{-0.10}$	$0.05^{+0.02}_{-0.02}$	1.11 ± 0.12	2.94 ± 0.25	4.75 ± 0.26
ZTF J2320+3750	$2.51^{+0.22}_{-0.22}$	$1.29^{+0.79}_{-0.42}$	$1.16^{+0.54}_{-0.35}$	$0.15^{+0.01}_{-0.01}$	0.68 ± 0.39	13.00 ± 0.49	11.74 ± 0.43
ZTF J2055+4651	$2.57^{+0.12}_{-0.13}$	$2.17^{+0.63}_{-0.41}$	$1.94^{+0.30}_{-0.36}$	$0.53^{+0.02}_{-0.01}$	0.432 ± 0.098	-3.33 ± 0.17	-5.16 ± 0.17

Note. Comparison of three methods for estimating distances to the sample of binaries, including a spectroscopic distance and two parallax-based distances. Note that the Bailer-Jones (Bailer-Jones et al. 2018) and 400 pc length scale (Kupfer et al. 2018) techniques depend on Gaia astrometry, while the spectroscopic distances are determined from the measured radii and temperatures of the objects. We also estimate the reddening, $E(g-r)$, for each system (Green et al. 2019) and present the measured Gaia parallax, $\bar{\omega}$, and proper motions, μ R.A. and μ decl., for each system.

parallax, $\bar{\omega}$. Nonetheless, we wish to emphasize that, when available, a precisely measured Gaia parallax is incredibly valuable, as this method of estimating distances arises from a simple geometric effect, whereas other techniques of estimating distance invoke more complicated model dependence. Here, we compare two approaches for estimating distances for the sample of ZTF short-period binaries using Gaia parallaxes, though the technique we ultimately use in this paper is the spectroscopic distance estimate described above.

The two parallax-based distance estimates presented in Table 4 use an exponentially decreasing space density prior as described in Bailer-Jones et al. (2018). An important element of this prior is that it invokes a characteristic length scale (note that this is not a scale height). The distances reported by Bailer-Jones et al. (2018) couple this prior with length scales derived from a model of the galaxy. However, this model has its shortfalls when considering a specific population of objects such as WDs, as it is purely geometric and intended to be relatively independent of the properties of stars, and thus is not an optimal choice for characterizing a subpopulation of stars where additional information is present. Notably, as illustrated in Table 4, the Bailer-Jones technique tends to yield large distances at low Galactic latitudes, where the characteristic length scale is significantly larger than at higher Galactic latitude. Because WDs are foreground objects and this length scale is estimated based on all of the stars in a region of the sky, this method likely overestimates distances in the Galactic plane for WD populations. The alternative method, adopted by Kupfer et al. (2018), invokes the same exponentially decreasing space density prior but assumes a 400 pc characteristic length scale for all sources based on WD population synthesis work, rather than a length scale dependent on sky position. We report estimates based on a modified version of this method, with the same maximum-likelihood measurement, but instead we use a 68% credible interval derived from the highest posterior density of our distribution to estimate the error bars.

3.6. Combined Analysis and Observed Characteristics

We conduct a combined analysis of the lightcurve modeling of each system and modeling of the phase-resolved spectroscopy in order to estimate the properties of the systems reported in Table 5. We conducted the combined analysis using the nested sampling package MULTINEST (Feroz et al. 2009). When sampling, we combined modeling of the lightcurve with priors on the temperature of the hotter component in each binary based on a spectroscopic fit, and for the single-lined systems, an additional constraint based on the measured radial velocity semiamplitude. For single-lined systems, we used the velocity semiamplitude constraint plus constraints on the mass ratio from ellipsoidal modulation to infer parameters for the system. For double-lined systems, we instead used the mass–radius relations described in Soares (2017) to constrain the system parameters, allowing us to infer masses from radii estimated using the lightcurve. The single-lined, eclipsing, and ellipsoidal variable ZTF J1946+3203 is an exception, as in this system we inferred masses from a combination of the radial velocity semiamplitude and the well-constrained inclination and mass ratio inferred from the lightcurve, as well as radii measurable by the eclipses. Thus, this system serves as an example of one with parameters that can be used in testing mass–radius relations. Note that we did not model the two AM CVn systems, ZTF J1905+3134 and ZTF J2228+4949, and that modeling of the mass-transferring system ZTF J0643+0318 is still underway.

3.7. LISA Signal-to-noise Ratio

In order to estimate the LISA gravitational-wave S/N, we adopt the same formalism as outlined by Burdge et al. (2019a, 2019b, which was based on the formalism outlined in Korol et al. 2017), correcting a factor of 2 error that was present in the previous estimates, resulting in overall lower S/N estimates. We use the updated sensitivity curve presented in Robson et al. (2019).

Table 5
Physical System Parameters

Quantity: Units:	M_A (M_\odot)	M_B (M_\odot)	R_A (R_\odot)	R_B (R_\odot)	T_A (kK)	T_B (kK)
ZTF J1539+5027 (1)	$0.610^{+0.017}_{-0.022}$	$0.210^{+0.015}_{-0.015}$	$0.01562^{+0.00038}_{-0.00038}$	$0.03140^{+0.00054}_{-0.00052}$	$48.9^{+0.9}_{-0.9}$	< 10
ZTF J0538+1953	$0.45^{+0.05}_{-0.05}$	$0.32^{+0.03}_{-0.03}$	$0.02069^{+0.00028}_{-0.00034}$	$0.02319^{+0.00032}_{-0.00026}$	$26.45^{+0.725}_{-0.725}$	$12.8^{+0.2}_{-0.2}$
PTF J0533+0209 (2)	$0.652^{+0.037}_{-0.040}$	$0.167^{+0.030}_{-0.030}$		$0.057^{+0.004}_{-0.004}$		$20^{+0.8}_{-0.8}$
ZTF J2029+1534	$0.32^{+0.04}_{-0.04}$	$0.30^{+0.04}_{-0.04}$	$0.029^{+0.002}_{-0.003}$	$0.028^{+0.003}_{-0.003}$	$18.25^{+0.25}_{-0.25}$	$15.3^{+0.3}_{-0.3}$
ZTF J0722–1839	$0.38^{+0.04}_{-0.04}$	$0.33^{+0.03}_{-0.03}$	$0.0224^{+0.0004}_{-0.0002}$	$0.0249^{+0.0001}_{-0.0003}$	$19.9^{+0.15}_{-0.15}$	$16.8^{+0.15}_{-0.15}$
ZTF J1749+0924	$0.40^{+0.07}_{-0.05}$	$0.28^{+0.05}_{-0.04}$	$0.022^{+0.003}_{-0.004}$	$0.025^{+0.004}_{-0.004}$	$20.4^{+0.2}_{-0.2}$	$12.0^{+0.6}_{-0.6}$
ZTF J1946+3203	$0.272^{+0.046}_{-0.043}$	$0.307^{+0.097}_{-0.085}$	$0.0299^{+0.0049}_{-0.0045}$	$0.111^{+0.012}_{-0.013}$	$11.5^{+2.3}_{-4.6}$	$28.0^{+1.7}_{-1.7}$
ZTF J0640+1738	$0.39^{+0.12}_{-0.089}$	$0.325^{+0.30}_{-0.15}$		$0.152^{+0.040}_{-0.032}$	$10.2^{+8.3}_{-6.8}$	$31.5^{+5.0}_{-5.0}$
ZTF J2130+4420 (3)	$0.545^{+0.020}_{-0.020}$	$0.337^{+0.015}_{-0.015}$		$0.125^{+0.005}_{-0.005}$		$42.4^{+3.0}_{-3.0}$
ZTF J1901+5309	$0.36^{+0.04}_{-0.04}$	$0.36^{+0.05}_{-0.05}$	$0.029^{+0.001}_{-0.002}$	$0.022^{+0.003}_{-0.002}$	$26.0^{+0.2}_{-0.2}$	$16.5^{+2.0}_{-2.0}$
ZTF J2320+3750	$0.69^{+0.03}_{-0.03}$	$0.20^{+0.01}_{-0.01}$		$0.152^{+0.015}_{-0.017}$		$9.2^{+0.2}_{-0.2}$
ZTF J2055+4651 (4)	$0.68^{+0.05}_{-0.05}$	$0.41^{+0.04}_{-0.04}$	$0.0148^{+0.002}_{-0.002}$	$0.17^{+0.01}_{-0.01}$	$63.0^{+1.0}_{-1.0}$	$33.7^{+1.0}_{-1.0}$

Note. Derived physical parameters for the components in our systems, including the masses of the two components, M_A and M_B , the radii of the components, R_A and R_B , and the effective surface temperatures of the components, T_A and T_B . We have excluded systems with significant mass transfer contributing to the luminosity: ZTF J0643+0318, ZTF J1905+3134, and ZTF J2228+4949. All were determined using the analyses described in Section 3, with the exception of ZTF J1539+5027, PTF J0533+0209, ZTF J2130+4420, and ZTF J2055+4651, whose parameters were taken from previous publications.

References. (1) Burdge et al. (2019a), (2) Burdge et al. (2019b), (3) Kupfer et al. (2020b), (4) Kupfer et al. (2020a).

For a more detailed discussion of LISA S/N estimates and their subtleties, please see the appendix.

4. Discussion of Individual Systems

4.1. ZTF J1539+5027

ZTF J1539+5027 is a deeply eclipsing DWD binary system with an orbital period of just ≈ 6.91 minutes (Burdge et al. 2019a) consisting of a cool He WD orbiting a heated CO WD. This is one of two systems in our sample with confirmed orbital decay and, thus, a precise measurement of its chirp mass (assuming the decay is due to energy loss to gravitational radiation). There is ongoing work to more precisely characterize this system using observations obtained with the high-speed photometer HiPERCAM (see the first panel in Figure 2) and the COS spectrograph on the Hubble Space Telescope. The system is among the highest-S/N LISA-detectable gravitational-wave sources known, and it presents a curious evolutionary puzzle, as the CO WD in the system has been heated to $\approx 50,000$ K, but there are no observational indications of active mass transfer (see Burdge et al. 2019a for further details).

4.2. ZTF J0538+1953

ZTF J0538+1953 is a 14.44 minute orbital period eclipsing detached DWD system. The hotter WD has $T_{\text{eff}} \approx 26,000$ K, and the cooler companion $\approx 13,000$ K. The two components are of comparable radii (with the cooler being slightly larger than its hot companion, indicating that it is likely the less massive component). The lightcurve exhibits a moderate degree of flux reprocessed by the heated face of the cooler WD in the system (causing an 8% peak-to-peak amplitude photometric modulation on the orbital period), though this effect is much smaller than that observed in ZTF J1539+5027. After conducting lightcurve modeling, we found a best fit for the mass ratio $q = \frac{M_B}{M_A} = 5.01 \pm 0.55$, where M_B corresponds to the mass of the cooler, larger secondary. This is highly unlikely because this physically conflicts with WD mass–radius relations (which were used to infer the final reported masses).

Upon further inspection of the residuals of the model, we see that even with the best-fit model, there is a residual signal with a few percent amplitude at twice the orbital frequency, phase-shifted with respect to the expected phase of ellipsoidal modulation. This signal could arise as a result of incomplete modeling of the reprocessed radiation on the heated face of the secondary or could potentially be indicative of a dynamically excited tidal pulsation, as is expected to occur at twice the orbital frequency in circular orbit systems. Further follow-up should allow us to understand this signal, but for the purposes of this work, we have omitted quoting a mass ratio of the object based on the lightcurve, as it is difficult to disentangle this signal from any weak ellipsoidal modulation that may be present.

ZTF J0538+1953 is perhaps best compared to SDSS J0651+2844, the 12.75 minute orbital period detached binary discovered by Brown et al. (2011) and further characterized in Hermes et al. (2012). ZTF J0538+1953’s components have measured R/a values of ≈ 0.11 for the hot $\approx 26,000$ K and ≈ 0.13 for the cooler $\approx 13,000$ K component, whereas the components of SDSS J0651+2844 have R/a values of ≈ 0.12 for the hotter object and ≈ 0.045 for the cooler, more compact companion.

Invoking mass–radius relations in combination with the lightcurve modeling (which makes use of the radii inferred from eclipses to determine masses), we find that the cooler component in ZTF J0538+1953 is consistent with a $0.32^{+0.03}_{-0.03} M_\odot$ object, suggesting it is a He WD. The hotter WD in the system has a mass consistent with a $0.45^{+0.05}_{-0.05} M_\odot$ object, which lies in a regime where the WD could be a He WD, CO WD, or hybrid WD (Perets et al. 2019).

4.3. ZTF J1905+3134

ZTF J1905+3134 is an AM CVn system exhibiting a photometric modulation at ≈ 17.2 minutes and strong double-peaked He II emission, similar to that seen in SDSS J1351–0643 (Green et al. 2018). Shorter orbital period AM CVn systems like SDSS J1351–0643 and ZTF J1905+3134 do not

normally undergo outbursts like their longer period counterparts, and instead they remain in a constant high state (Ramsay et al. 2018), and ZTF J1905+3134’s strong He II emission is characteristic of shorter period systems in the high state. The photometric modulation in this system could either originate from the orbital period or the disk precession period (Green et al. 2018); however, the KPED lightcurve of the object illustrated in Figure 2 shows a deep, sharp temporal feature, which suggests that the system is eclipsing (with a possible additional eclipse of a hot spot shortly after the deeper eclipse), which would make this the shortest orbital period eclipsing AM CVn known. Further photometric follow-up of this faint system could constrain these features more precisely, but current follow-up (which consists of just a few orbital cycles) lacks the S/N necessary for detailed modeling. ZTF J1905+3134 is the only object in our sample that completely lacks a Gaia astrometric solution, so we instead refer to Ramsay et al. (2018) in order to estimate the distance based on its luminosity and the period–luminosity relation for AM CVn systems. AM CVn systems around the period range of 17 minutes exhibit absolute luminosity values in the range of $M_G \approx 5\text{--}8$. Thus, using a uniform prior on the absolute luminosity reflecting this range, and comparing to the Gaia apparent magnitude of $G = 20.90 \pm 0.030$, we estimate that the object lies approximately 3.8–9.55 kpc from the Sun.

4.4. PTF J0533+0209

PTF J0533+0209 is a ≈ 20.6 minute orbital period detached binary system first described in Burdge et al. (2019b). The system is unique due to its He-dominated DBA atmosphere, which exhibits only traces of hydrogen, a previously unseen characteristic among ELM WDs. The system’s atmospheric composition raises a question about formation channels because it requires fine-tuning of evolutionary models to produce an object with so little hydrogen (see Burdge et al. 2019b for further details). Like ZTF J1539+5027, orbital decay has been detected in this system, enabling the measurement of a chirp mass assuming an orbital evolution that is primarily due to general relativity. The system houses an unseen compact object, likely a CO WD.

4.5. ZTF J2029+1534

ZTF J2029+1534 is a detached eclipsing DWD binary with an orbital period of ≈ 20.9 minutes. With relatively large R/a values of ≈ 0.15 and ≈ 0.12 and temperatures of $\approx 18,000$ K and $\approx 15,000$ K, respectively, this system likely consists of two similar-temperature He WDs, with mass–radius relations giving estimated masses of $0.32^{+0.04}_{-0.04} M_\odot$ and $0.30^{+0.04}_{-0.04} M_\odot$ for the two components, respectively. The system is among the faintest in the sample, with a Pan-STARRS g -band apparent magnitude of ≈ 20.4 .

4.6. ZTF J0722–1839

ZTF J0722–1839 is a detached eclipsing DWD binary with an orbital period of ≈ 23.70 minutes. Remarkably, the primary and secondary eclipses in this system both result in an attenuation of nearly half of the system’s flux (with the deeper eclipse attenuating slightly over 50% of the flux, and the secondary eclipse over 40% of the flux). The nearly equal-depth eclipses indicate that the objects must be able to almost

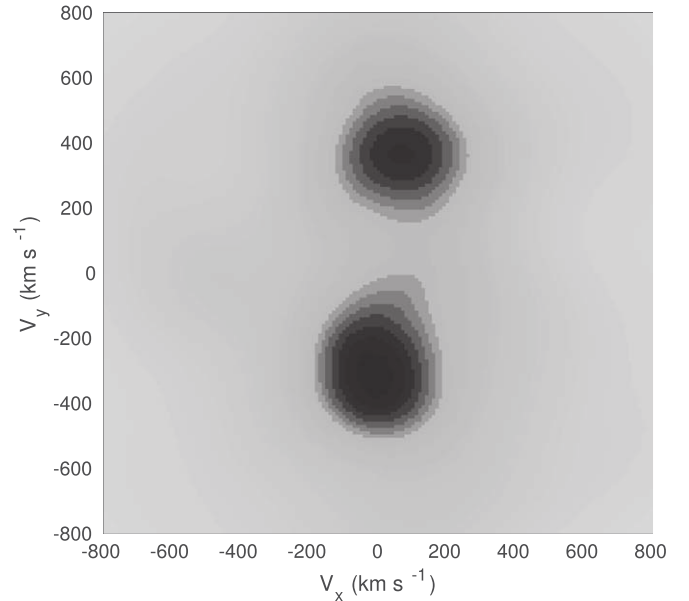


Figure 5. Doppler tomogram (Marsh 2001) of the Balmer series of absorption lines in ZTF J0722–1839. The two dark features correspond to absorption line cores tracking each object, reflecting the system’s double-lined nature.

completely occult each other, indicating similar radii, and their nearly equal depths indicate nearly equal luminosity per unit surface area, implying similar temperatures for the two WDs. Finally, to achieve such deep eclipses, the system must also be near edge-on. Based on the system parameters reported in Table 3, we infer that this system is a double He WD system, with two He WDs of similar temperatures and radii. This may imply that the two objects have similar ages, requiring a formation mechanism capable of producing the two objects in rapid succession. Figure 5 illustrates a Doppler tomogram (Marsh 2001) of the Balmer series of hydrogen absorption lines in this spectrum. The two distinct features visible in the tomogram correspond to distinct absorption lines originating from the two WDs, illustrating that this system is double-lined. However, due to the shallow topographical nature of these features in the tomogram (as a result of overall low-S/N spectra in each phase bin), the velocities of the two components are poorly constrained with the current set of spectra; however, further spectroscopic follow-up of this system is underway, as it is clearly a promising candidate for measuring dynamical masses, which would serve as a test of WD mass–radius relations. Further work is underway to measure precise dynamical masses in this system.

4.7. ZTF J1749+0924

ZTF J1749+0924 was the final discovery in the sample described in this paper, identified using the BLS algorithm. The system likely consists of a pair of eclipsing He WDs with an orbital period of approximately 26.4 minutes. ZTF observed this system in a continuous cadence mode (taking exposures with an approximately 40 s cadence continuously for an hour and a half, on two separate occasions). On both occasions of continuously sampled observations by ZTF, the system exhibited multiple eclipses during the observation window (with each “eclipse” having only a single detection due to the

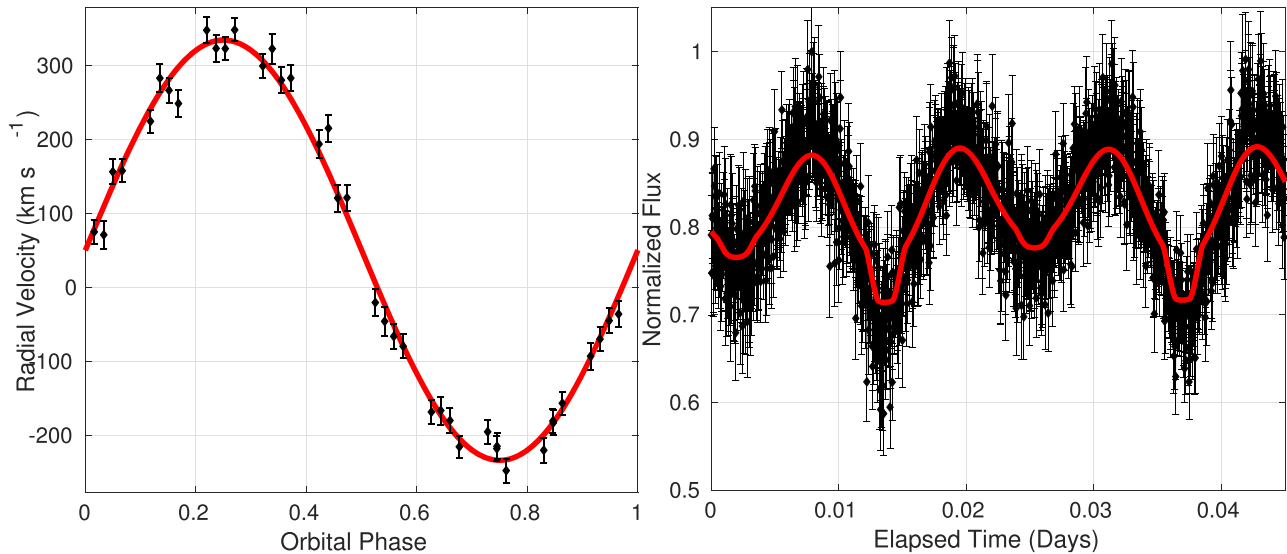


Figure 6. Left panel: radial velocities of ZTF J1946+3203 as measured from phase-resolved spectra obtained with LRIS (black points). The smearing-corrected measured semi-amplitude for this system is $284.8 \pm 4.8 \text{ km s}^{-1}$, with the sinusoidal fit shown in red. Right panel: best-fit model (red) to the CHIMERA *g*-band lightcurve of the system (black points), which exhibits both strong ellipsoidal modulation and an eclipse. The presence of ellipsoidal modulation, eclipses, and a clearly measured radial velocity semi-amplitude allowed us to measure both component masses and radii, which we have determined likely reveal a double He WD binary system. The data in this figure is the same as shown in Figures 2 and 4 and is meant to illustrate an example model fit to the data used in parameter estimation.

short duty cycle of the feature). The system likely contains a pair of He WDs, with masses of $0.40_{-0.05}^{+0.07} M_{\odot}$ and $0.28_{-0.04}^{+0.05} M_{\odot}$.

4.8. ZTF J2228+4949

ZTF J2228+4949 is an AM CVn system whose spectrum exhibits the double-peaked He II emission characteristic of a hot accretion disk, much like that seen in ZTF J1905+3134. The system exhibits a photometric modulation at ≈ 28.56 minutes; compared to other high-state AM CVn systems (Ramsay et al. 2018), ZTF J2228+4949 has an unusually long period. We propose that this system may be the longest-period high-state AM CVn system known, potentially due to an unusually high accretion rate at its orbital period. In any case, our survey, which targets systems displaying strong optical periodicity, is naturally biased toward systems in a persistent high state, as they are more likely to exhibit photometric modulation due to the presence of a superhump (Green et al. 2018) and also do not undergo outbursts, which can greatly impact the ability to search for periods. We estimate a spectroscopic distance of 0.72–1.77 kpc, based on the typical absolute magnitude of AM CVns at these periods falling in the range $M_G \approx 8$ –10. Because ZTF J2228+4949 may have an unusually high accretion rate for its period, it is possible that the source is more distant than this spectroscopic estimate. A more precise distance estimate not based on the system’s luminosity would be particularly valuable, as it would allow one to constrain whether the luminosity is indeed elevated compared to other sources at comparable orbital periods.

4.9. ZTF J1946+3203

ZTF J1946+3203 is a single-lined spectroscopic eclipsing binary that shows strong ellipsoidal variations, as is clearly apparent in the CHIMERA lightcurve shown in Figure 6. The more luminous component in this system has a surface temperature of approximately $28,000 \pm 2000 \text{ K}$ and a DAB atmosphere exhibiting both H and He I lines, with a

spectroscopically measured surface gravity of $\log(g) = 5.74 \pm 0.2$. A combined analysis of the lightcurve and radial velocities yields mass estimates of $0.272_{-0.043}^{+0.046} M_{\odot}$ for the less luminous component (likely a He WD), and a mass of $0.307_{-0.085}^{+0.097} M_{\odot}$ for the more luminous component (which could be consistent with either a hot He WD or an sdB). Systems like ZTF J1946+3203 are particularly valuable, as they exhibit eclipses, ellipsoidal variations, and an unambiguous radial velocity semi-amplitude, strongly constraining component masses, temperatures, and radii.

4.10. ZTF J0643+0318

ZTF J0643+0318 is a single-lined spectroscopic eclipsing binary undergoing mass transfer and consequently exhibiting a strong He II emission feature. Further work is underway to characterize this system.

4.11. ZTF J0640+1738

ZTF J0640+1738 is a single-lined spectroscopic binary exhibiting ellipsoidal modulation. The atmosphere of its more luminous component exhibits helium lines in addition to hydrogen, much like an sdB. Based on its large radius and high temperature, the system is likely a WD+sdB system. Because degenerate He WDs pass through the same location in color–luminosity space as sdBs, it is difficult to differentiate the two classes of objects. The parameters for this system are poorly constrained, due to the absence of a high-quality follow-up lightcurve. Further follow-up is underway to better constrain this system’s characteristics.

4.12. ZTF J2130+4420

ZTF J2130+4420 is a mass-transferring WD+sdB system described in Kupfer et al. (2020b). When the high-S/N HiPERCAM lightcurve of the system was modeled, the shape of the primary minimum in the lightcurve could only be

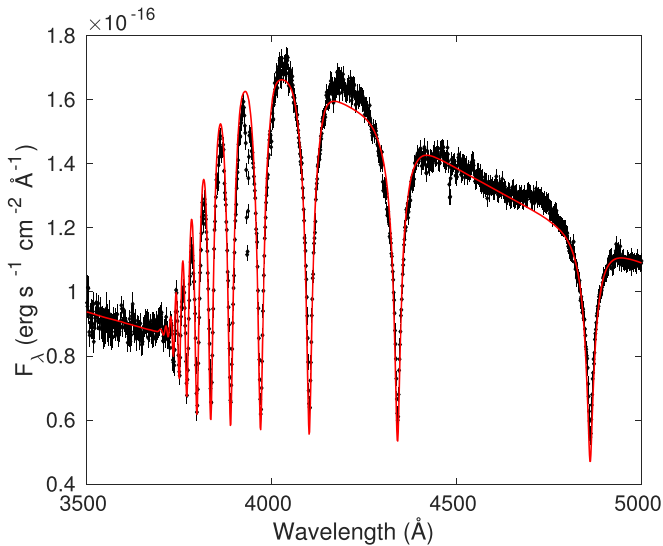


Figure 7. Coadded and dereddened LRIS spectrum of ZTF J2320+3750 (black points), fit with a spectroscopic model (red) to determine the surface temperature and gravity of the white dwarf.

reproduced with an accretion disk eclipsing the sdB in the system (which dominates the luminosity). The lightcurves of J2130+4420 and of the similar system J2055+4651 are very distinctive, with minima of different depths, making them easy to identify as ellipsoidal/eclipsing variables and distinguish them from other periodic variables in this period range.

4.13. ZTF J1901+5309

ZTF J1901+5309 is an eclipsing pair of He WDs described in detail in Coughlin et al. (2019). While the core composition of the WDs is ambiguous due to the system being a double-lined spectroscopic binary, we have determined masses using mass–radius relations for the two components and identified both as consistent with He WDs.

4.14. ZTF J2320+3750

ZTF J2320+3750 consists of a CO WD orbiting a He WD. The He WD exhibits a spectrum similar to other ELMs, including a Mg II metal line (ELMs often show enhanced photospheric abundances of metals, which has been attributed to a combination of rotational mixing and radiative levitation; see Kaplan et al. 2013; Hermes et al. 2014). The LRIS spectrum of ZTF J2320+3750 with an example of the model used to fit it is illustrated in Figure 7. Notably, ZTF J2320+3750 has a large radial velocity semiamplitude for its orbital period. Large-scale, massively multiplexed spectroscopic surveys should be quite sensitive to detecting single-lined systems such as ZTF J2320+3750 and others described in this work with multiple observations.

4.15. ZTF J2055+4651

ZTF J2055+4651 is a mass-transferring and eclipsing WD +sdB system described in Kupfer et al. (2020a). The system has a lightcurve that is incredibly similar to that of ZTF J2130+4420, with minima of very different depths, making it easily distinguishable from other variables such as δ Scuti pulsators. The high-S/N HiPERCAM lightcurve revealed a weak eclipse

of the donating sdB star by a massive WD accretor, implying an accretor temperature of over 60,000 K (see Kupfer et al. 2020a for further details).

5. Discussion

5.1. Selection Biases

In order to determine what underlying population of objects our sample represents, we must consider selection biases introduced when identifying objects based on photometric periodicity and color. By selecting objects with the colors satisfying Pan-STARRS $(g - r) < 0.2$ and $(r - i) < 0.2$, our survey probes a large color space, effectively selecting all objects with $T > 6700$ K. Because our selection was a simple color cut, the objects in our sample span a large dynamic range in absolute luminosity, ranging from DWDs to systems containing helium stars. The selection does omit cool objects ($T < 6700$ K), and the cool secondary of ZTF J1539+5027 suggests the possibility that tides may not efficiently heat all WDs at short orbital periods (Burdge et al. 2019a), suggesting that there may be value in extending the selection to encompass a cooler sample of objects as well.

Binary systems containing a high-temperature component are prone to exhibiting pronounced eclipses and are intrinsically more luminous than their cool counterparts, allowing us to probe a larger volume on average by targeting blue systems than if we simply selected objects at all colors. Less-luminous, cool WDs do outnumber hot WDs, meaning that the space density of short-period DWDs could be substantially larger than that of the high-temperature systems we are targeting if WDs in close binaries are not efficiently heated by tides. We believe our omission of cool WDs is unlikely to have significantly diminished the number of DWDs detectable in ZTF, because WDs are intrinsically faint due to their small size, and cool WDs fall below the ZTF’s detection threshold at much closer distances than their hot counterparts, greatly limiting the volume that can be probed in the cool temperature regime (consider a $0.3 M_{\odot}$ He WD at 6700 K: such an object would have an apparent magnitude of 21 in g at a distance of just 430 pc, and a $0.6 M_{\odot}$ CO-core WD at this temperature would reach this apparent magnitude at just 270 pc).

We also searched the entire catalog of WD candidates reported in Gentile Fusillo et al. (2019), which includes cooler WDs, and we discovered no binary candidates that were not already encompassed by the Pan-STARRS color cut. Like the Pan-STARRS color cut, in this work we only report binary systems with under 1 hr orbital period recovered by the search. Of the 486,641 WDs in this catalog, 248,246 had over 50 epochs in ZTF. Of the 15 systems described here, ZTF J0538+1953, PTF J0533+0209, ZTF J0722–1839, ZTF J2228+4949, ZTF J0640+1738, ZTF J1901+5309, and ZTF J2320+3750 are members of the Gentile Fusillo et al. (2019) WD catalog.

In contrast to optical surveys, gravitational-wave surveys like LISA are agnostic to the temperatures of sources and thus will probe this cooler population of binaries, which remain hidden to optical surveys. Sources with luminous, nondegenerate helium star components such as ZTF J0643+0318, ZTF J2130+4420, and ZTF J2055+4651 are intrinsically luminous enough that they can exceed ZTF’s detection threshold at several kiloparsecs, even when heavily extinguished, as is the case for both ZTF J0643+0318 and ZTF J2055+4651. Thus, by

targeting redder sources, one could potentially expect to find more such systems.

We did not employ any selection invoking the astrometric solutions of the Gaia survey (Gaia Collaboration et al. 2018) because ZTF’s limiting apparent magnitude of ≈ 21 is beyond the threshold of Gaia’s ability to measure reliable parallaxes. Additionally, ZTF has acquired a significant amount of photometry in dense regions of the Galactic plane, where Gaia astrometric solutions are less reliable than in fields with lower density and higher galactic latitude.

Curiously, of the eclipsing systems in our sample, only one contains a clear $>0.5 M_{\odot}$ WD, even though the ELM survey found primarily pairs of He-core+CO-core WDs. However, this is easily understood as a selection effect. In general, CO WDs are less luminous than their He WD counterparts because of their smaller size. Thus, when such systems do undergo eclipses, it results in a shallow eclipse, as the CO WD subtends a small cross section of the larger He WD companion when it occults it. During the secondary eclipse when the CO WD is occulted, little luminosity is lost, as the CO WD only contributes a small fraction of the total luminosity of the system (unless the CO WD is significantly hotter than the He WD, as is the case in ZTF J1539+5027).

Objects discovered via ellipsoidal modulation carry a different selection effect. As discussed in Faulkner et al. (1972), there is a direct relation between the density of an object and the orbital period at which it overflows its Roche lobe, with only a weak dependence on mass ratio. In cases where the companion has a higher mass than the object overflowing its Roche lobe ($q < 1$, as is necessarily the case for most double-degenerate objects exhibiting ellipsoidal modulation), one can relate the orbital period at which the object fills its Roche lobe, P_b , in days, and the density ρ of the Roche-filling object in g cm^{-3} with the useful approximation

$$P_b \approx \frac{0.43}{\rho^{1/2}}, \quad (6)$$

which does not deviate by more than 3% for $1 < q < 100$ (Eggleton 1983). The selection effect introduced by this relation is quite apparent: photometric surveys like ZTF only detect ellipsoidal modulation in objects nearly filling their Roche lobes, and therefore they can only detect such binaries in a narrow range of orbital periods, governed by the lower-density component in the system. Consequentially, high-density objects such as CO WDs can only be discovered at extremely short orbital periods using ellipsoidal modulation, as these objects do not begin to fill their Roche lobes until $P_b \approx 1$ minute. At these orbital periods, gravitational radiation acts so quickly that the merger timescale of the systems is short (less than 500 yr for a pair of $0.6 M_{\odot}$ CO WDs at 60 s orbital period, which would exhibit ellipsoidal modulation on the order of a few percent at this period). However, selecting targets that exhibit ellipsoidal modulation does not introduce significant bias regarding the mass of the unseen companion, other than the basic requirement that it should be more dense or less luminous than the detected object (otherwise it would be the object dominating the signal). This has already manifested itself in our small sample of objects, as several of the systems exhibiting ellipsoidal modulation contain higher-mass and presumably CO-core WDs, such as ZTF J2320+3750 and

ZTF J0533+0209, whereas the majority of the eclipsing systems contain pairs of He WDs.

In conclusion, it is unsurprising, based on selection biases, that our sample contains systems with at least one low-mass He WD or a nondegenerate He star component, as detecting ellipsoidal modulation or eclipses is challenging for systems containing only CO WDs or more compact objects. Notably, the location of our sample when plotted on a Hertzsprung–Russell diagram shown in Figure 8 reflects this, as all systems are clearly overluminous relative to the WD cooling track. It is worth noting that detecting objects via photometry has important advantages over spectroscopic selection in that obtaining spectra requires dividing photons across many pixels, and thus requires integrating for much longer to exceed the signal per pixel necessary to avoid significant dilution of the S/N by readout noise. This means that spectroscopic surveys must either target significantly brighter objects than a photometric survey or sacrifice critical temporal resolution by acquiring longer exposures than a photometric survey of equivalent depth. Such considerations are important when comparing massively multiplexed spectroscopic surveys and photometric surveys like ZTF and their discovery potential in the phase space of short-orbital-period binaries.

5.2. LISA

Our survey targets binary systems with orbital periods under an hour because LISA’s gravitational-wave sensitivity peaks in this regime. Figure 9 shows the characteristic strain of ZTF and ELM samples of compact binaries and LISA’s sensitivity. As illustrated in Figure 9, half of our sample falls above the LISA sensitivity curve after 4 yr of observations, though the current uncertainty in LISA S/N for most sources originates from an uncertainty in the distance to the sources. It is also worth noting that the characteristic strains plotted in Figure 9 are a quantity that does not account for inclination, and as discussed earlier, a near edge-on inclination significantly diminishes the gravitational-wave signal expected from a binary compared to a face-on system. Many of the ZTF sources consist of two He-core WDs, whereas the ELM survey is dominated by He WDs orbiting higher-mass CO-core counterparts, with the notable exception of the system reported in Brown et al. (2020a), meaning that on average the chirp mass is lower in the ZTF sample of objects than in the ELM survey.

The average orbital period of the systems in the ZTF sample is significantly shorter than in the ELM sample, due both to selection criteria (this work did not pursue objects with $P_b > 60$ minutes) and selection bias, as eclipses and ellipsoidal modulation become more difficult to detect at longer periods, though future work will characterize longer-period systems. Shorter-period objects like ZTF J1539+5027 have a small lifetime (see Table 6) and are thus rarer, and they are likely to be more distant if detected at all.

As illustrated in Figure 9, targeting objects at short periods compensates for the loss in characteristic strain that is due to such systems being rarer (and thus more distant), as LISA’s sensitivity increases by more than an order of magnitude over the period range of objects in our sample. The increase in sensitivity from LISA couples with the $f^{2/3}$ frequency dependence of the gravitational-wave amplitude and the boost in S/N due to $\sqrt{N_{\text{cycle}}}$ over 4 yr of observations, meaning that the characteristic strain scales as $f^{7/6}$. Thus, a system like ZTF

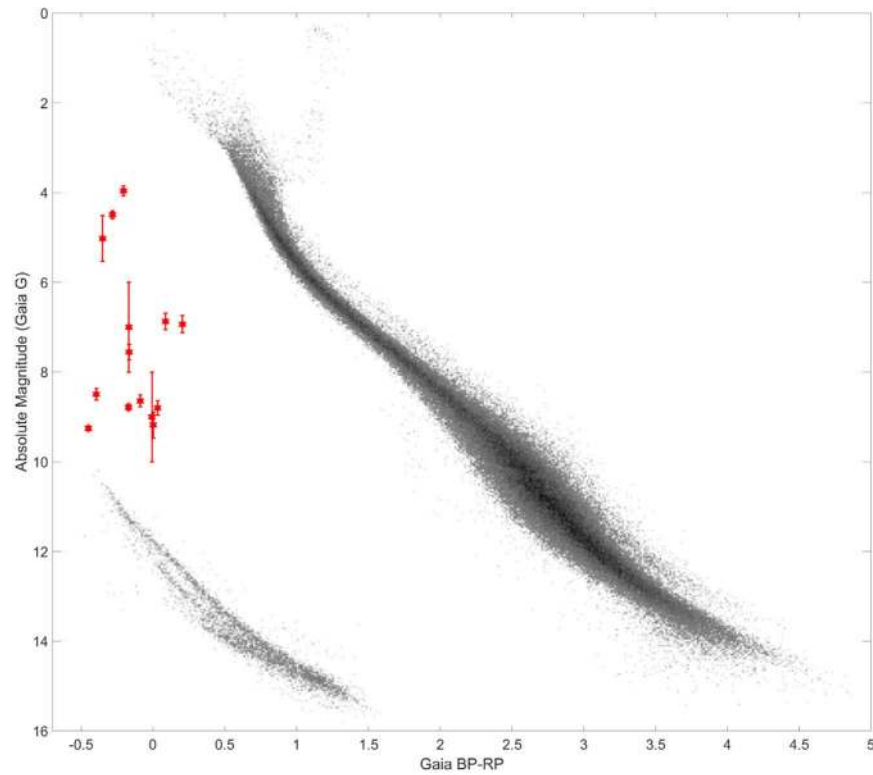


Figure 8. Hertzsprung–Russell diagram illustrating the dereddened locations of 14 binaries in the sample with spectroscopic distances (ZTF J0643+0318 is omitted, as its modeling is ongoing). The red stars represent objects that are in our sample, with absolute luminosities calculated based on their spectroscopic distances. Most objects cluster between absolute magnitudes of 6.5 and 10.0, with the exception of the systems containing either He-burning stars or young and hot He WDs (which contribute significant additional luminosity, dwarfing both the luminosity of the companion WD and any accretion luminosity). The background color–magnitude diagram (CMD) is the sample of all stars in Gaia within 100 pc that have reliable astrometric solutions.

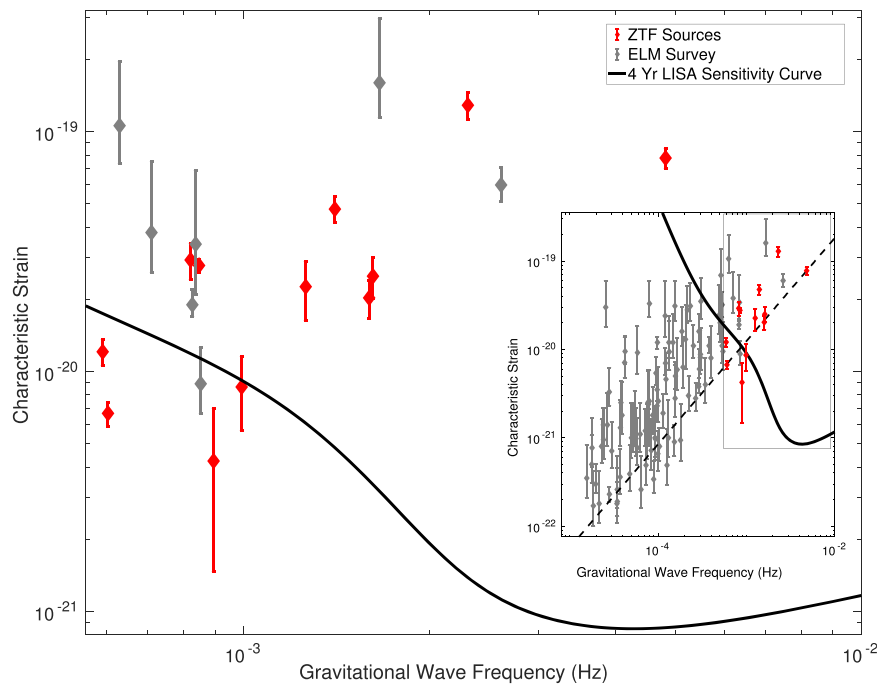


Figure 9. Characteristic gravitational-wave strain of the sources described in this work (shown as red diamonds; note that the three mass-transferring sources for which we do not yet have parameter estimates have been omitted), compared with the sample of DWD binaries from the ELM survey (shown as gray diamonds), overplotted with the 4 yr LISA sensitivity curve (solid black line). An inset compares the sample presented in this paper (which exclusively investigated systems with orbital periods under an hour), with the full sample of systems discovered by the ELM survey (Brown et al. 2020b). The inset also presents the evolution of ZTF J1539+5027 with the dashed black line, illustrating what its characteristic strain would have been in the past at longer orbital periods. Overall, the ZTF sample contains two high-S/N gravitational-wave sources (ZTF J1539+5027 and ZTF J0538+1953, with 4 yr S/Ns of approximately 96). See Table 6 for further details. The 4 yr LISA sensitivity curve was computed as described in Robson et al. (2019).

Table 6
LISA S/N of Systems

Name	4 yr LISA S/N	\mathcal{A}	$2 \cos(i)$	$1 + \cos^2(i)$	Decay Timescale (Myr)
ZTF J1539+5027	~ 96	$(9.96 \pm 0.93) \times 10^{-23}$	0.204 ± 0.022	1.0104 ± 0.0023	0.20753 ± 0.00043
ZTF J0538+1953	~ 96	$(2.38 \pm 0.30) \times 10^{-22}$	0.1593 ± 0.0031	1.00635 ± 0.00024	1.42 ± 0.17
PTF J0533+0209	~ 8	$(5.5 \pm 1.1) \times 10^{-23}$	0.591 ± 0.046	1.087 ± 0.014	3.89 ± 0.95
ZTF J2029+1534	~ 5	$(4.52 \pm 0.78) \times 10^{-23}$	0.117 ± 0.024	1.0034 ± 0.0014	5.35 ± 0.85
ZTF J0722-1839	~ 8	$(1.13 \pm 0.14) \times 10^{-22}$	0.0119 ± 0.0076	1.000036 ± 0.000050	5.95 ± 0.71
ZTF J1749+0924	~ 3	$(5.7 \pm 1.5) \times 10^{-23}$	0.158 ± 0.049	1.0062 ± 0.0039	9.1 ± 2.1
ZTF J1946+3203	< 1	$(2.46 \pm 0.80) \times 10^{-23}$	0.447 ± 0.055	1.050 ± 0.012	23 ± 11
ZTF J0640+1738	< 1	$(9.2 \pm 3.8) \times 10^{-24}$	0.83 ± 0.19	1.174 ± 0.079	...
ZTF J2130+4420	~ 2	$(8.47 \pm 0.53) \times 10^{-23}$	0.127 ± 0.035	1.0040 ± 0.0022	16.6 ± 8.1
ZTF J1901+5309	~ 2	$(9.05 \pm 0.15) \times 10^{-23}$	0.095 ± 0.017	1.00226 ± 0.00083	24.5 ± 3.8
ZTF J2320+3750	< 1	$(1.58 \pm 0.18) \times 10^{-23}$	0.19 ± 0.11	1.009 ± 0.012	55.8 ± 3.1
ZTF J2055+4651	< 1	$(4.42 \pm 0.51) \times 10^{-23}$	0.233 ± 0.017	1.0136 ± 0.0020	30.9 ± 3.3

Note. The sky and inclination-dependent estimated LISA S/Ns of all systems in our sample (we marginalize over polarization angle), after 4 yr of observations. All values are calculated using spectroscopic distances (see Table 4) and the characteristic decay timescale assuming gravitational-wave decay, defined as $\frac{3}{8} \frac{P_b}{|P_b|}$. As a point of comparison, we estimate SDSS J0651+2844 will reach an S/N of ~ 88 after 4 yr (with $M_A = 0.49 M_\odot$, $M_B = 0.247 M_\odot$, and $d = 0.933$ kpc). We have omitted estimates for the mass-transferring systems for which we do not have parameter estimates, and we have omitted a decay timescale estimate for ZTF J0640+1738 because of uncertainties larger than the estimate. The gravitational wave amplitude is defined as $\mathcal{A} = \frac{2(GM)^{5/3}}{c^4 d} (\pi f)^{2/3}$, and $2 \cos(i)$ and $1 + \cos^2(i)$ give the inclination-dependent coefficients of the two gravitational-wave polarizations, h_+ and h_\times , respectively.

J1539+5027 has an enormous advantage in detectability by LISA over a higher chirp mass system such as J2055+4651.

The most significant contributions of our survey to the sample of LISA-detectable binary systems are ZTF J1539+5027 and ZTF 0538+1953, which along with SDSS J0651+2844 form a trio of high-S/N eclipsing LISA-detectable binaries. Due to their eclipses, we can precisely time these systems using optical data, and thus given a few months to years of monitoring, we can measure orbital decay with high confidence and potentially even measure the acceleration of orbital decay.

Many of our binaries have precisely constrained inclinations as a result of features in their lightcurves (in particular those systems exhibiting eclipses). Eventually, these systems will serve as a test of LISA, which can also measure inclinations in systems through the ratio of the amplitudes of the two gravitational-wave polarizations, which have differing inclination dependence. The cross polarization, h_\times , scales as $(1 + \cos^2(i))$, whereas the plus polarization, h_+ , scales as $\cos(i)$, thus vanishing for the edge-on inclination, which most eclipsing systems are near. Ellipsoidal variables like PTF J0533+0209 stand to benefit significantly from a LISA gravitational-wave signal, which can be used to precisely constrain the inclination of these systems. When combined with the radial velocity semiamplitude and photometric ellipsoidal modulation amplitude, this allows for a robust estimate of the component masses.

When LISA begins to operate, we will gain new information on the sources. For a system like ZTF J1539+5027, which is already well constrained electromagnetically (but is also a high-S/N LISA source), the primary new constraint will be a precise distance estimate. Currently, this estimate is based on the measured radius and temperature of the object (known as a spectroscopic distance estimate), but such an estimate is model dependent and assumes a reliable understanding of variables such as extinction along the line of sight. LISA will provide a precisely measured gravitational-wave strain amplitude, and the chirp mass is already well estimated for this system based

on electromagnetic constraints, so one can infer the distance to the source using this amplitude. For some sources, particularly those that are ellipsoidal variables with well-measured temperatures, this precise distance measurement will help further constrain the properties of the system by placing tight constraints on the optical luminosity of the system.

Perhaps one of the most exciting class of systems LISA will detect are those like ZTF J1539+5027 but also bright enough to have their distances measured precisely via parallax. With such sources, one could use the gravitational-wave strain amplitude to precisely measure the chirp mass of the system in a robust manner. Such a measurement would be extremely exciting, as these systems have precisely measurable orbital decay rates from eclipse timing (or even if they lack optical periodicity to measure this from, LISA could be used to measure the frequency evolution of the system). One could use such systems to directly measure the difference in measured \dot{P}_b from that expected due to general relativity, probing the efficiency of tides in the system. Currently, the only system in our sample that has a distance measured precisely enough for such an exercise is ZTF J2130+4420, which unfortunately is a rather low-S/N LISA source. Additionally, this system is undergoing mass transfer, so any measured deviation of the orbital evolution from general relativity could be influenced by an exchange of angular momentum that is due to mass transfer.

5.3. Evolutionary Fates

All of the binaries in our sample are either already interacting or will interact in the near astronomical future (see Table 6). Thus, a significant question worth posing is what will occur when these systems interact. We illustrate possible outcomes in Figure 10 should the systems merge, based on the work described in Shen (2015).

Most of the double He WD systems in our sample are close to a mass ratio of unity, and thus are likely to merge when they interact (Marsh et al. 2004). As discussed in Shen (2015), these

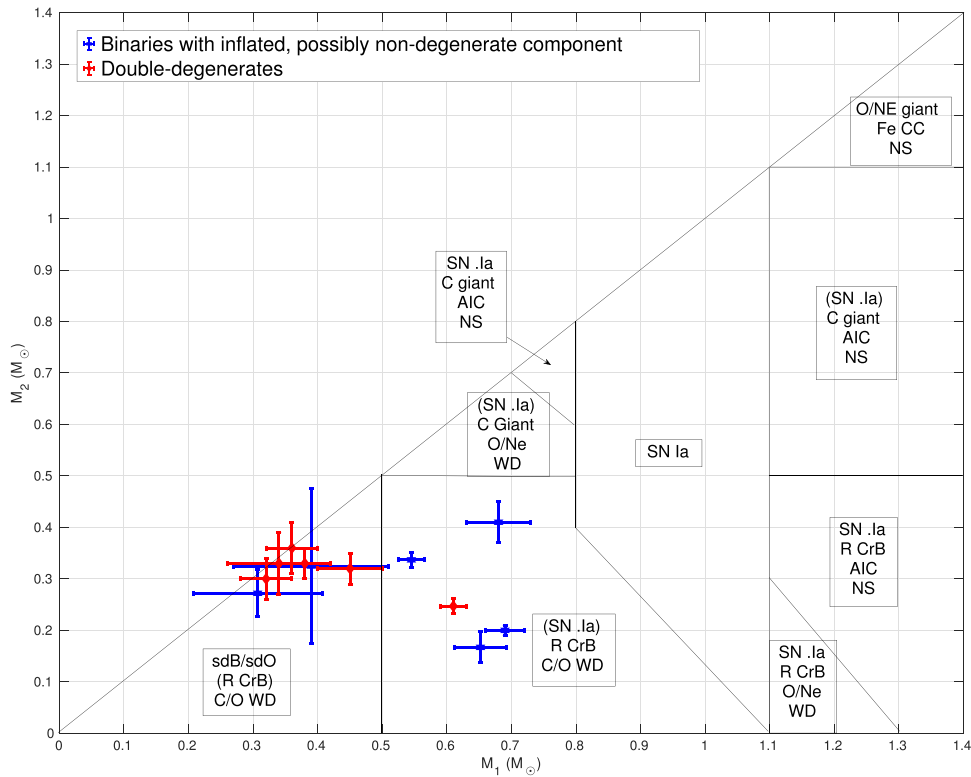


Figure 10. Reproduction of the diagram featured in Shen (2015), illustrating possible evolutionary fates of double-degenerate pairs. In red, we plot the double-degenerate objects discovered by our survey. Most of these are double He WDs that are expected to evolve into hot subdwarf star (sdB/sdO) objects upon merger. Three other double-degenerate systems (including ZTF J1539+5027) have CO cores and likely produce R CrB stars upon merger, though they could also turn into mass-transferring AM CVn systems that exhibit SN .Ia He-shell detonations. Systems containing nondegenerate objects (blue points) would only follow the scenarios described in Shen (2015) if the He-burning objects transitioned to a degenerate state prior to merger. They could produce other phenomena, including SNe Ia, due to mass transfer/merger before becoming degenerate (see text).

systems could evolve into two classes of objects: either a nondegenerate He-burning hot subdwarf star, which eventually cools into a CO WD, or alternatively, if they are in fact not He WDs but hybrids of low-mass CO WDs, they could form an R CrB star, which would also eventually cool into a CO WD. In either case, these systems ultimately end up on the WD track and thus serve as evidence that it is likely that at least some low-mass WDs merge and ultimately form a CO WD.

The other double-degenerate systems in the sample, containing both a CO WD and a He WD, have larger mass ratios than double He WD systems. Thus, with the onset of mass transfer, it is possible that these systems could evolve into AM CVns (Ramsay et al. 2018). However, Shen (2015) proposes that these systems too could ultimately merge and along the way potentially produce powerful helium detonations known as .Ia (“dot Ia”) supernovae. Upon merger, they are expected to form an R CrB as the He WD is disrupted by its more dense CO companion, forming a helium atmosphere around this core. Ultimately, most of these R CrB stars would cool to form a CO WD on the WD cooling track.

Finally, the remaining systems in our sample contain a degenerate WD accreting from a nondegenerate He-burning star (ZTF J2130+4420 and ZTF J2055+4651). These systems will likely build up a layer of helium on the CO WD, which could eventually undergo a detonation, and if the CO WD is sufficiently massive, this could result in a “double detonation” by igniting the degenerate carbon–oxygen core (Shen et al. 2018a, 2018b). However, in the case of ZTF J2130+4420, the CO WD is only $0.545_{-0.020}^{+0.020} M_{\odot}$, likely too low even to produce

a subluminous SN Ia, whereas ZTF J2055+4651, with its $0.68_{-0.05}^{+0.05} M_{\odot}$, is the more likely of the two objects to produce such an event (Perets et al. 2019). Ultimately, the two objects could also exhaust helium shell burning and simply cool into double degenerates. Upon merger, they would likely form a rapidly rotating CO WD, potentially preceded by an R CrB phase if substantial He remains, as expected for hybrid WDs (Perets et al. 2019). For further details on these systems, please see Kupfer et al. (2020a, 2020b).

6. Conclusion

Using data from the ZTF, we have significantly increased the number of known binary systems with an orbital period of less than one hour. Using high-speed photometric follow-up in combination with spectroscopic follow-up, we have characterized the physical parameters of the systems using model-dependent techniques invoking WD mass–radius relations. In future work, we hope to obtain more model-independent measurements such as orbital decay rates to more robustly characterize the physical parameters of these systems.

We will continue to analyze ZTF data as it accumulates more epochs and discovers more such objects. At the current stage of the survey, the sample we have discovered exhibits a remarkably high fraction of pairs of He WDs, likely due to selection effects. As we continue the survey, we anticipate discovering more systems and that our discoveries will begin to include other classes of sources, such as pairs of CO WDs. All of the detached systems in our sample should be undergoing

rapid orbital decay due to general relativity, and we expect to detect this orbital decay in every detached system with high significance before LISA launches.

The algorithms and analysis techniques we are developing will be applicable to upcoming surveys such as the one that will be conducted by the Vera Rubin Observatory (LSST Science Collaboration et al. 2009). These data sets will be accompanied by their own challenges (in particular, lower cadence, split across many filters). Given the clear promise demonstrated by the discoveries emerging from ZTF, we are optimistic that optical time-domain surveys will continue to revolutionize our understanding of binaries in the millihertz regime. These surveys will set the stage for LISA, having discovered dozens, if not hundreds, of sources by the time the instrument begins to operate (Korol et al. 2017). In future work, we will characterize our recovery efficiency in greater detail using synthetic lightcurves, in order to better characterize ZTF’s sensitivity to detecting the population of DWDs in the galaxy. Efforts are currently underway to increase sensitivity to the shortest-period binary systems by accounting for their orbital period evolution, which requires algorithms that can accommodate acceleration searches (Katz et al. 2020).

Binaries with compact object components are transitioning into a golden age, as we enter an era when time-domain surveys such as ZTF enable detection via periodic features. Massively multiplexed spectroscopic surveys acquiring multiple epochs such as SDSS-V (Kollmeier et al. 2017) and LAMOST (Cui et al. 2012) will enable detection of these systems via large radial velocity shifts, with the feasibility of this technique having already been demonstrated on a smaller scale by the ELM survey, as well as the SWARMS survey (Badenes et al. 2009). Deep all-sky X-ray surveys such as that being conducted by the eROSITA instrument on board the SRG mission (Merloni et al. 2012) will enable detection of ultracompact X-ray binaries and direct-impact accreting systems such as HM Cancri (Roelofs et al. 2010). Finally, Gaia (Gaia Collaboration et al. 2018) has completely revolutionized stellar astronomy by providing parallax measurements, which has enabled careful targeting of objects such as WDs. This era will culminate with the launch of LISA, which will enable detection of thousands of these systems in the form of gravitational waves and revolutionize our understanding of compact binary systems.

K.B.B. thanks the National Aeronautics and Space Administration and the Heising-Simons Foundation for supporting his research.

M.W.C. acknowledges support from the National Science Foundation with grant No. PHY-2010970.

P.R.-G. acknowledges support from the State Research Agency (AEI) of the Spanish Ministry of Science, Innovation and Universities (MCIU), and the European Regional Development Fund (FEDER) under grant AYA2017–83383–P.

V.S.D., ULTRACAM, and HiPERCAM are supported by STFC.

The research leading to these results has received funding from the European Research Council under the European Union’s Horizon 2020 research and innovation program numbers 677706 (WD3D) and 340040 (HiPERCAM).

This work is based on observations obtained with the Samuel Oschin Telescope 48 inch and the 60 inch Telescope at the Palomar Observatory as part of the Zwicky Transient Facility

project. ZTF is supported by the National Science Foundation under grant No. AST-1440341 and a collaboration including Caltech, IPAC, the Weizmann Institute for Science, the Oskar Klein Center at Stockholm University, the University of Maryland, the University of Washington, Deutsches Elektronen-Synchrotron and Humboldt University, Los Alamos National Laboratories, the TANGO Consortium of Taiwan, the University of Wisconsin at Milwaukee, and Lawrence Berkeley National Laboratories. Operations are conducted by COO, IPAC, and UW.

This work is based on observations made with the Gran Telescopio Canarias (GTC) installed in the Spanish Observatorio del Roque de los Muchachos of the Instituto de Astrofísica de Canarias, in the island of La Palma.

This work is based on observations made at the European Southern Observatory New Technology Telescope (NTT), La Silla.

The KPED team thanks the National Science Foundation and the National Optical Astronomical Observatory for making the Kitt Peak 2.1 m telescope available. The KPED team thanks the National Science Foundation, the National Optical Astronomical Observatory, and the Murty family for support in the building and operation of KPED. In addition, they thank the CHIMERA project for use of the Electron Multiplying CCD (EMCCD).

Some of the data presented herein were obtained at the W.M. Keck Observatory, which is operated as a scientific partnership among the California Institute of Technology, the University of California, and the National Aeronautics and Space Administration. The observatory was made possible by the generous financial support of the W.M. Keck Foundation. The authors wish to recognize and acknowledge the very significant cultural role and reverence that the summit of Maunakea has always had within the indigenous Hawaiian community. We are most fortunate to have the opportunity to conduct observations from this mountain.

This article is based on observations made in the Observatorios de Canarias del IAC with the William Herschel Telescope operated on the island of La Palma by the Isaac Newton Group of Telescopes in the Observatorio del Roque de los Muchachos.

This research benefited from interactions at the ZTF Theory Network Meeting that were funded by the Gordon and Betty Moore Foundation through grant GBMF5076 and support from the National Science Foundation through PHY-1748958.

Facilities: PO:1.2 m (ZTF), KPNO:2.1 m (KPED), NTT (ULTRACAM), Hale (CHIMERA, DBSP), GTC (HiPERCAM), Keck:I (LRIS).

Appendix A

Instrumental/Observational Information

A.1. LRIS

We obtained the majority of our spectroscopic follow-up using the LRIS (Oke et al. 1995) on the 10 m W.M. Keck I Telescope on Maunakea. We conducted most of our observations using the 600 grooves mm^{-1} grism with a blazing angle of 4000 Å and the 1" slit on the spectrograph, resulting in an effective FWHM resolution of 3.8–4.1 across the wavelength range of the blue arm (the approximate wavelength range is 3200–5800 Å). The dispersion of this element results in approximately 0.63 Å of wavelength per pixel, meaning that

we sample the point-spread function from this slit with more than six unbinned pixels, so we always bin along the dispersion axis when observing with this instrument, as it significantly reduces readout time and read noise and comes with no cost in resolving power (at least in the case of 2×2 binning). For some observations that required particularly short exposures (such as ZTF J1539+5027), we binned 4×4 to further reduce readout time. Ultimately, the lower limits of exposure times during spectroscopic observations are set by the readout duty cycle and read noise floor (one splits photons across many pixels when obtaining spectra, resulting in a small number of counts per pixel, which can quickly become comparable to the readout noise in short exposures). Frame-transfer CCDs offer an attractive solution to eliminating the readout duty-cycle bottleneck (which, for observing ZTF J1539+5027, for example, was a prohibitive 34%, as the effective exposure time was 52 s, but even with 4×4 binning, the readout time was still 27 s). Electron-multiplying CCDs take this one step further by offering both the possibility of eliminating the issue of readout time and also eliminating read noise, meaning that observations can be obtained in photon-counting mode. The catch of such an instrument is a factor of $\sqrt{2}$ larger readout noise due to coincidence losses (Tulloch & Dhillon 2011); however, for faint targets that require high temporal resolution, these CCDs offer a solution that conventional CCDs do not. Coincidence losses can be avoided in the photon-counting limit where no more than one photon is incident on a pixel in any given image, making this technology particularly attractive for higher resolution CCDs where the dispersion is sufficiently high that this regime can be easily reached.

A.2. DBSP

We obtained the spectrum of ZTF J2228+4949 using the Double-Beam Spectrograph (DBSP; Oke & Gunn 1982) on the 200 inch Hale telescope at Palomar observatory. The instrument provides a resolution comparable to LRIS and has similar limitations in readout-time overheads. We used the 600 grooves mm^{-1} grating and the 1" slit.

A.3. ISIS

Spectra for ZTF J2130+4420 were obtained using the ISIS spectrograph on the 4.2 m William Herschel Telescope. For further details on these observations, please see Kupfer et al. (2020b).

A.4. GMOS-N

Spectra for ZTF J2055+4651 were obtained using the GMOS-N spectrograph on the 8.1 m Gemini North Telescope. For further details on these observations, please see Kupfer et al. (2020a).

A.5. HiPERCAM

HiPERCAM is a high-speed photometer mounted on the 10.4 m Gran Telescopio Canarias (GTC) on the island of La Palma in the Canary Islands (Dhillon et al. 2018; V. Dhillon et al. 2020, in preparation). The instrument is a frame-transfer quintuple-beam imager, allowing for simultaneous imaging in

the u , g , r , i , and z bands at frame rates of >1 kHz. The light-collecting power of a 10 m class telescope, combined with the high frame rate of this instrument, makes it optimal in obtaining the high-S/N observations of the systems described in this work, particularly systems such as ZTF J1539+5027, whose eclipse ingress and egress last only a few seconds and span an apparent magnitude range of approximately 21 in g at the start of the eclipse and reach >27 in g at the base of the eclipse.

A.6. ULTRACAM

ULTRACAM is a three-channel high-speed photometer currently mounted on the 3.5 m New Technology Telescope at La Silla observatory (Dhillon et al. 2007). All observations on this instrument were conducted using u and g filters on two of the channels, and the remaining channel either the r or i band. Like the other high-speed photometers used in our observations, the instrument is operated in frame-transfer mode, effectively eliminating the readout duty cycle.

A.7. CHIMERA

The Caltech High-speed Multi-color camERA (CHIMERA; Harding et al. 2016) is a dual-channel high-speed photometer mounted on the prime focus of the 200 inch Hale telescope at Palomar Observatory. CHIMERA consists of a pair of electron-multiplying CCDs capable of using either conventional amplifiers or those with electron-multiplying gain. We operated the detectors in the conventional amplifier mode with frame transfer enabled, as for all of our targets we obtained enough photons in several-second exposures such that the $\sqrt{2}$ increase in shot noise from using the electron-multiplying gain would erase any gains from eliminating readout noise.

A.8. KPED

The Kitt Peak Electron Multiplying CCD Demonstrator (KPED) is a single-channel high-speed photometer mounted on the 2.1 m telescope at Kitt Peak National Observatory (Coughlin et al. 2019). The instrument uses the same electron-multiplying CCDs used by CHIMERA. The observations highlighted in this work were obtained using frame-transfer mode and in g .

Appendix B Period Finding

In this section, we explore the sensitivity of the algorithms used to discover the systems described in this work using both a real example and synthetic signals.

We typically search approximately 2 million trial frequencies per lightcurve. The highest frequency we search to is 720 times per day, and the lowest is defined as $2/\text{baseline}$, where the baseline is the end date of the lightcurve, minus the start. Because the frequency grid depends on the baseline of the lightcurve, we compute it independently for each lightcurve. We used an oversampling factor of 4. To avoid aliases due to the sidereal day, we slice frequencies out of the frequency grid at 1.0 day and its various harmonics.

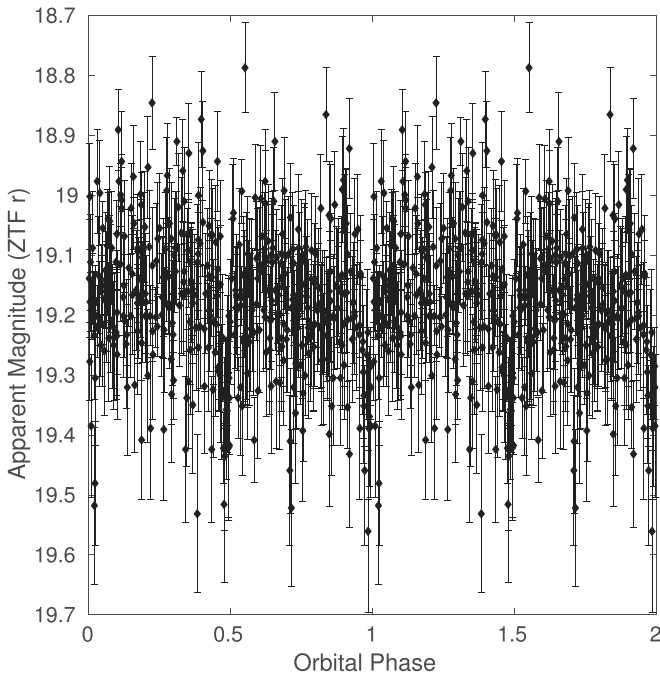


Figure 11. Phase-folded ZTF lightcurve of the 12.75 minute orbital period binary SDSS J0651+2844 (Brown et al. 2011), which we blindly recover with our period-finding algorithms. An early dedicated observation of this system during ZTF’s commissioning served as a proof of concept that a wide-field optical time-domain survey such as ZTF could function as a powerful tool for identifying members of this class of gravitational-wave source.

One of the known systems we tested our technique on was the 12.75 minute binary system SDSS J0651+2844 (Brown et al. 2011), whose phase-folded ZTF lightcurve is illustrated in

Figure 11. This system did not become recoverable in the main ZTF survey until over 600 epochs had been accumulated (see Figure 12 for further details), as its eclipses are quite shallow because the more luminous component is the larger. We expect that as ZTF’s sampling continues to increase, we should start to recover more eclipsing CO WD plus He WD white dwarf systems like SDSS J0651+2844, whereas our current discoveries in general exhibit larger photometric amplitudes than seen in SDSS J0651+2844 because they consist primarily of pairs of He WDs, or as in the case of ZTF J1539+5027, the more compact CO WD dominates the luminosity.

In Figure 12 we illustrate the sensitivity of the conditional entropy algorithm to both a sinusoidal signal and a square wave as a function of both the amplitude of the signal and the number of epochs. In addition to characterizing the sensitivity of the algorithm to a synthetic signal, we also present ZTF’s median rms scatter as a function of apparent magnitude and the cumulative ZTF sampling of Gaia objects above a decl. of -28° in Figure 12. Using this figure, one can, for example, infer that at an apparent magnitude of 19, ZTF has an rms scatter of $\approx 7\%$, and approximately two-thirds of all sources in Gaia above a decl. of -28° have 500 or more detections in ZTF at this apparent magnitude. Using the top panels of the figure, one can then estimate that ZTF should have detected more than half of all sinusoidal sources at this apparent magnitude with an amplitude of $>3.5\%$. These are crude estimates, and further work is underway to conduct careful simulations of ZTF data to better characterize detection efficiency by accounting for the cadence in each field, data artifacts, and other important elements that the simple treatment presented below cannot capture. The work presented in this publication is not intended to explore rates, so we leave the analysis at this.

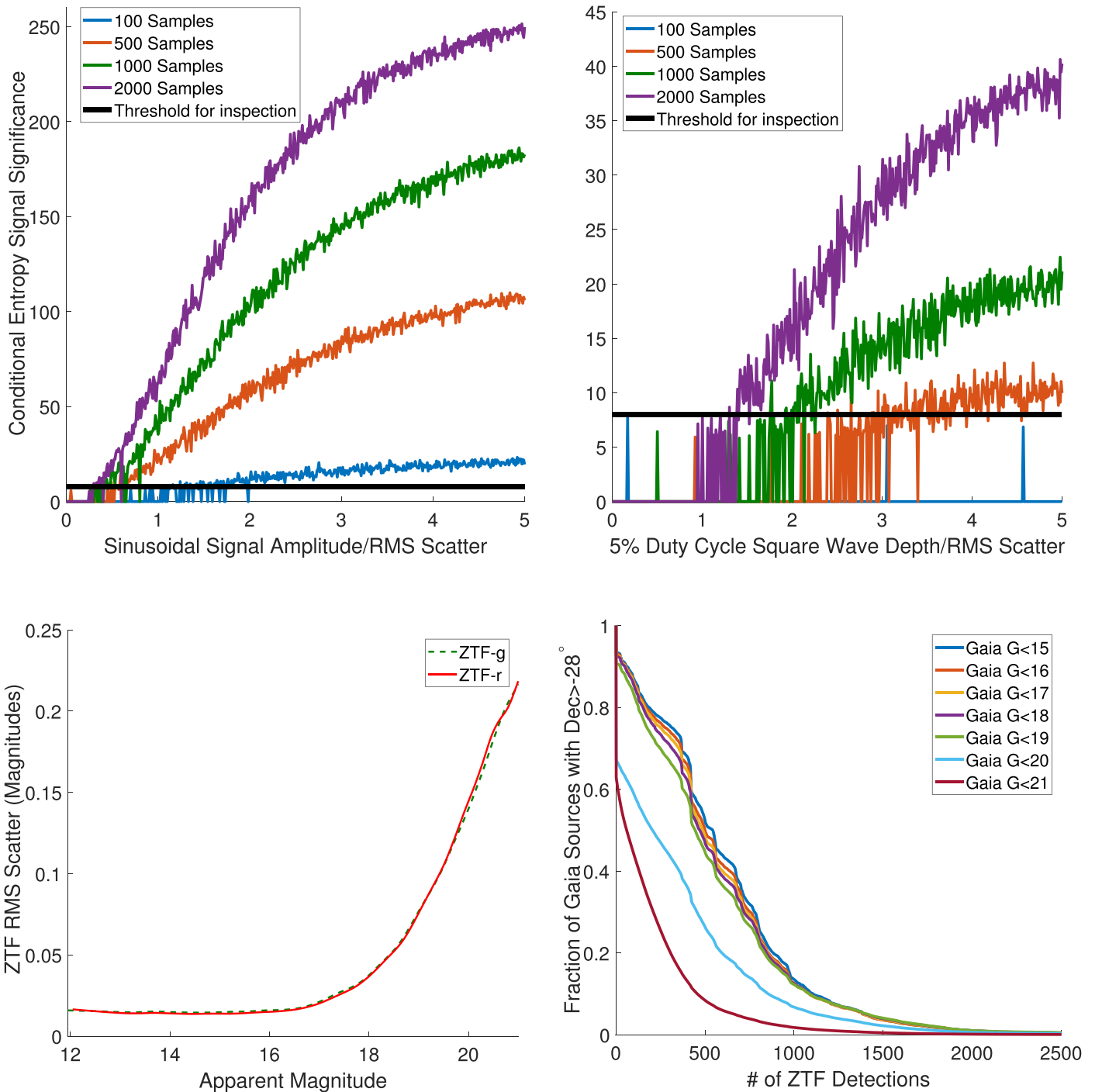


Figure 12. Upper left: the significance returned by the conditional entropy algorithm on a synthetic sinusoidal signal with a 10 minute period. On the x -axis, we illustrate the semi-amplitude of the sinusoid compared to the rms scatter injected into the signal. The horizontal black line illustrates the significance threshold we imposed to inspect lightcurves visually for candidates. Upper right: This panel is analogous to the upper left panel, but rather than a synthetic sinusoidal signal, the algorithm was instead run on a synthetic eclipsing signal in the form of a periodic square wave with a 10 minute period and 5% duty cycle. Lower left: an empirical average of ZTF’s rms scatter for a sample of all Gaia sources with a color of $(BP - RP) < 0.5$. Lower right: an illustration of the fraction of Gaia sources with $\text{decl.} > -28^\circ$ and with a color of $(BP - RP) < 0.5$ vs. the number of archival ZTF photometric detections of these sources. The large number of faint sources with no detections is dominated by sources that were not detected in the ZTF reference image used to seed the archival database (primarily located in dense regions of the Galactic plane). See Masci et al. (2019) for further details.

Appendix C LISA Signal-to-noise Ratio

Here, we walk through the basic formalism we used to estimate the S/Ns of the binaries in this paper.

In order to estimate the LISA gravitational-wave S/N, we adopt the same formalism as outlined in Robson et al. (2019).

In Burdge et al. (2019a, 2019b), the chirp mass, M_c , was estimated from the rate of orbital decay that is due to gravitational-wave emission. In this work, we do not yet have precise orbital-decay measurements of any other systems, so we instead estimate the chirp mass from mass estimates based on lightcurve and spectroscopic modeling. We use the

Table 7
Observations of Systems Used in Analyses in This Publication

Name	Instrument	Observation Dates (UTC)	Configuration	Frame Exptime
ZTF J1539+5027	LRIS	2018 Jun 16, Jul 12, 13	600 grooves mm ⁻¹ grism, 4 × 4 binning	52 s
	HiPERCAM	2019 Jun 2, 4, 5	<i>u, g, r, i, z</i>	6, 3, 3, 6, 9 s
ZTF J0538+1953	LRIS	2019 Sep 3, 27	600 grooves mm ⁻¹ grism, 4 × 4 binning	90 s
	HiPERCAM	2019 Sep 4, 8	<i>u, g, r, i, z</i>	3, 1, 1, 3, 4 s
ZTF J1905+3134	LRIS	2019 Jul 5	400 grooves mm ⁻¹ grism, 2 × 2 binning	300 s
	KPED	2019 Jul 3	<i>g</i>	10 s
PTF J0533+0209	LRIS	2017 Nov 15, 2018 Mar 19	400 grooves mm ⁻¹ grism, 2 × 2 binning	120 s
	CHIMERA	2017 Dec 14, 15	<i>g, i</i>	10 s
PTF J2029+1534	LRIS	2020 Mar 21	600 grooves mm ⁻¹ grism, 2 × 2 binning	120 s
	CHIMERA	2019 Oct 1	<i>g, r</i>	3, 3 s
ZTF J0722–1839	LRIS	2019 Apr 5, 6, 2020 Feb 17	600 grooves mm ⁻¹ grism, 2 × 2 binning	141 s
	ULTRACAM	2020 Jan 26	<i>u, g, i</i>	12, 6, 6 s
ZTF J1749+0924	LRIS	2020 Mar 21	600 grooves mm ⁻¹ grism, 2 × 2 binning	120 s
	CHIMERA	2020 Jul 15	<i>g, r</i>	5, 5 s
ZTF J2228+4949	DBSP	2019 Jul 31	600 grooves mm ⁻¹ grating	200 s
ZTF J1946+3203	LRIS	2019 Sep 27	600 grooves mm ⁻¹ grism, 2 × 2 binning	168 s
	CHIMERA	2019 Aug 6	<i>g, i</i>	3, 3 s
ZTF J0643+0318	LRIS	2020 Jan 25	600 grooves mm ⁻¹ grism, 2 × 2 binning	170 s
	ULTRACAM	2019 Sep 28	<i>u, g, i</i>	24, 8, 8 s
ZTF J0640+1738	LRIS	2019 Feb 17	600 grooves mm ⁻¹ grism, 2 × 2 binning	157 s
ZTF J2130+4420	ISIS	2019 Jun 25, 26	R300B grating	120 s
	HiPERCAM	2019 Jul 8	<i>u, g, r, i, z</i>	3.54, 1.77, 1.77, 1.77, 3.54 s
ZTF J1901+5309	LRIS	2019 Sep 3	600 grooves mm ⁻¹ grism, 2 × 2 binning	141 s
	CHIMERA	2019 Aug 8	<i>g, i</i>	3, 3 s
ZTF J2320+3750	LRIS	2019 Sep 27	600 grooves mm ⁻¹ grism, 2 × 2 binning	138 s
	CHIMERA	2020 Jul 15	<i>g, r</i>	5, 5 s
ZTF J2055+4651	GMOS-N	2019 Sep 24, 25	B600 grating	180 s
	HiPERCAM	2019 Jul 8	<i>u, g, r, i, z</i>	9, 3, 3, 3, 9 s

approximation for the orbit-averaged signal amplitude at the detector computed in Cornish & Larson (2003),

$$A^2 = \mathcal{A}^2((1 + \cos^2(i))^2 \langle F_+^2 \rangle + 4 \cos^2(i) \langle F_\times^2 \rangle), \quad (\text{C1})$$

where the intrinsic source amplitude is given by $\mathcal{A} = \frac{2(GM)^{5/3}}{c^4 d} (\pi f)^{2/3}$, and the orbit-averaged detector responses are $\langle F_+^2 \rangle$ and $\langle F_\times^2 \rangle$ (see Cornish & Larson 2003 for the full expressions of these quantities). Note that Cornish & Larson (2003) include a factor of $\frac{1}{2}$ in this expression, which we have omitted. This factor of $\frac{1}{2}$ arises from time averaging over the $|\cos(\psi t)|^2$ in the signal; however, in order to find agreement with the sky, inclination, and polarization averaged S/N in Robson et al. (2019), we found we had to eliminate this $\frac{1}{2}$. We believe this is because in Robson et al. (2019), the phase of the gravitational wave is expressed as $e^{i\psi t}$, and when Robson et al. (2019) compute the inner product of the gravitational wave with itself, this term vanishes.

To estimate the S/N, we use the expression given in Korol et al. (2017):

$$S/N^2 = \frac{A^2 T_{\text{obs}}}{P_n(f_s)}, \quad (\text{C2})$$

where $P_n(f_s)$ is the power spectral density of the noise in a Michelson channel. We obtain the sky-averaged LISA noise curve from Robson et al. (2019). In order to estimate the power spectral density of the noise, we divide the sky-averaged sensitivity by the sky-averaged response function, $\sqrt{3/20}$, to

obtain an effective non-sky-averaged curve (see Robson et al. 2019 for further details). Note that while the response function given in Robson et al. (2019) is $\sqrt{3/10}$, it is actually a composite of a response that arises from averaging over the sky (the $\sqrt{3/20}$) and an additional factor of $\sqrt{2}$ that arises from summing over two independent channels, which we want to preserve in our S/N estimate.

The S/N described in this work is simply an estimate that uses a time-averaged approximation, and it is not a substitute for a full time-dependent LISA simulation. Our estimates do account for sky location and inclination, as these parameters are well constrained for the sources in this work and do have significant impacts on the estimated S/N. For the purposes of our S/N estimates, we marginalized over the polarization angle. We repeated our calculations using the waveforms given in Robson et al. (2019), and we arrived at the same estimated S/Ns using these combined with the orbit-averaged signal (we compute the orbital-averaged response in Equation (C2), using the waveforms given by Robson et al. 2019 Equation (15), with the amplitude given by Robson et al. 2019 Equation (20); we use this quantity as the expectation value of the numerator in Robson et al. 2019 Equation (36); and we arrive at the same result as the formalism outlined above).

Combined with a distance and inclination estimate, knowing the chirp mass allows for a direct estimate of the gravitational-wave strain of the source as measured from Earth. We report the estimated LISA S/N for the sources in the sample in Table 6.

It is worth noting that these S/Ns are a factor of $\sqrt{2}$ different than those presented in Korol et al. (2017) and Burdge et al. (2019a, 2019b), due to an error that introduced a factor of two

into the strain amplitude, in combination with a $\sqrt{\frac{1}{2}}$ from the prefactor of $\frac{1}{2}$ we omitted in Equation (C1) in this work (which was not omitted in previous work). We also used the more up-to-date LISA sensitivity given in Robson et al. (2019), which changed results at the $\sim 10\%$ level compared to the sensitivity of Amaro-Seoane et al. (2017).

ORCID iDs

Kevin B. Burdge  <https://orcid.org/0000-0002-7226-836X>
 Thomas A. Prince  <https://orcid.org/0000-0002-8850-3627>
 Jim Fuller  <https://orcid.org/0000-0002-4544-0750>
 David L. Kaplan  <https://orcid.org/0000-0001-6295-2881>
 Thomas R. Marsh  <https://orcid.org/0000-0002-2498-7589>
 Pier-Emmanuel Tremblay  <https://orcid.org/0000-0001-9873-0121>
 Zhuyun Zhuang  <https://orcid.org/0000-0002-1945-2299>
 Eric C. Bellm  <https://orcid.org/0000-0001-8018-5348>
 Ilaria Caiazzo  <https://orcid.org/0000-0002-4770-5388>
 Michael W. Coughlin  <https://orcid.org/0000-0002-8262-2924>
 Vik S. Dhillon  <https://orcid.org/0000-0003-4236-9642>
 Boris Gaensicke  <https://orcid.org/0000-0002-2761-3005>
 Pablo Rodríguez-Gil  <https://orcid.org/0000-0002-4717-5102>
 Matthew J. Graham  <https://orcid.org/0000-0002-3168-0139>
 JJ Hermes  <https://orcid.org/0000-0001-5941-2286>
 Thomas Kupfer  <https://orcid.org/0000-0002-6540-1484>
 S. P. Littlefair  <https://orcid.org/0000-0001-7221-855X>
 Przemek Mróz  <https://orcid.org/0000-0001-7016-1692>
 E. S. Phinney  <https://orcid.org/0000-0002-9656-4032>
 Jan van Roestel  <https://orcid.org/0000-0002-2626-2872>
 Yuhan Yao  <https://orcid.org/0000-0001-6747-8509>
 Richard G. Dekany  <https://orcid.org/0000-0002-5884-7867>
 Dmitry A. Duvv  <https://orcid.org/0000-0001-5060-8733>
 George Helou  <https://orcid.org/0000-0003-3367-3415>
 Ashish. A. Mahabal  <https://orcid.org/0000-0003-2242-0244>
 Frank J. Masci  <https://orcid.org/0000-0002-8532-9395>
 Reed Riddle  <https://orcid.org/0000-0002-0387-370X>
 Roger Smith  <https://orcid.org/0000-0001-7062-9726>
 Maayane T. Soumagnac  <https://orcid.org/0000-0001-6753-1488>
 S. R. Kulkarni  <https://orcid.org/0000-0001-5390-8563>

References

- Amaro-Seoane, P., Audley, H., Babak, S., et al. 2017, arXiv:1702.00786
 Badenes, C., Mullally, F., Thompson, S. E., & Lupton, R. H. 2009, *ApJ*, 707, 971
 Bailer-Jones, C. A. L., Rybizki, J., Foesneau, M., Mantelet, G., & Andrae, R. 2018, *AJ*, 156, 58
 Bellm, E. C., Kulkarni, S. R., Graham, M. J., et al. 2019, *PASP*, 131, 018002
 Benacquista, M. J. 2011, *ApJL*, 740, L54
 Bloemen, S., Marsh, T. R., Degroote, P., et al. 2012, *MNRAS*, 422, 2600
 Breger, M. 2000, in ASP Conf. Ser. 210, δ Scuti Stars (Review), ed. M. Breger & M. Montgomery (San Francisco, CA: ASP), 3
 Brinkworth, C. S., Burleigh, M. R., Lawrie, K., Marsh, T. R., & Knigge, C. 2013, *ApJ*, 773, 47
 Brown, W. R., Gianninas, A., Kilic, M., Kenyon, S. J., & Allende Prieto, C. 2016, *ApJ*, 818, 155
 Brown, W. R., Kilic, M., Allende Prieto, C., Gianninas, A., & Kenyon, S. J. 2013, *ApJ*, 769, 66
 Brown, W. R., Kilic, M., Allende Prieto, C., & Kenyon, S. J. 2010, *ApJ*, 723, 1072
 Brown, W. R., Kilic, M., Allende Prieto, C., & Kenyon, S. J. 2012, *ApJ*, 744, 142
 Brown, W. R., Kilic, M., Bédard, A., Kosakowski, A., & Bergeron, P. 2020a, *ApJL*, 892, L35
 Brown, W. R., Kilic, M., Hermes, J. J., et al. 2011, *ApJL*, 737, L23
 Brown, W. R., Kilic, M., Kosakowski, A., et al. 2020b, *ApJ*, 889, 49
 Brown, W. R., Kilic, M., Kosakowski, A., & Gianninas, A. 2017, *ApJ*, 847, 10
 Burdge, K. B., Coughlin, M. W., Fuller, J., et al. 2019a, *Natur*, 571, 528
 Burdge, K. B., Fuller, J., Phinney, E. S., et al. 2019b, *ApJL*, 886, L12
 Chambers, K. C., Magnier, E. A., Metcalfe, N., et al. 2016, arXiv:1612.05560
 Charpinet, S., Fontaine, G., Brassard, P., & Dorman, B. 1996, *ApJL*, 471, L103
 Claret, A. 2000, *A&A*, 363, 1081
 Claret, A., Cukanovaite, E., Burdge, K., et al. 2020a, *A&A*, 634, A93
 Claret, A., Cukanovaite, E., Burdge, K., et al. 2020b, arXiv:2007.15715
 Copperwheat, C. M., Marsh, T. R., Dhillon, V. S., et al. 2010, *MNRAS*, 402, 1824
 Cornish, N. J., & Larson, S. L. 2003, *PhRvD*, 67, 103001
 Coughlin, M. W., Dekany, R. G., Duvv, D. A., et al. 2019, *MNRAS*, 485, 1412
 Cui, X.-Q., Zhao, Y.-H., Chu, Y.-Q., et al. 2012, *RAA*, 12, 1197
 Dekany, R., Smith, R. M., Riddle, R., et al. 2020, *PASP*, 132, 038001
 Dhillon, V., Dixon, S., Gamble, T., et al. 2018, *Proc. SPIE*, 10702, 107020L
 Dhillon, V. S., Marsh, T. R., Stevenson, M. J., et al. 2007, *MNRAS*, 378, 825
 Eggleton, P. P. 1983, *ApJ*, 268, 368
 Faulkner, J., Flannery, B. P., & Warner, B. 1972, *ApJL*, 175, L79
 Feroz, F., Hobson, M. P., & Bridges, M. 2009, *MNRAS*, 398, 1601
 Fontaine, G., & Brassard, P. 2008, *PASP*, 120, 1043
 Fuller, J., & Lai, D. 2012, *MNRAS*, 421, 426
 Fuller, J., & Lai, D. 2013, *MNRAS*, 430, 274
 Gaia Collaboration, Brown, A. G. A., Vallenari, A., et al. 2018, *A&A*, 616, A1
 Geier, S., Østensen, R. H., Nemeth, P., et al. 2017, *A&A*, 600, A50
 Gentile Fusillo, N. P., Tremblay, P.-E., Gänsicke, B. T., et al. 2019, *MNRAS*, 482, 4570
 Gianninas, A., Dufour, P., Kilic, M., et al. 2014, *ApJ*, 794, 35
 Gianninas, A., Kilic, M., Brown, W. R., Canton, P., & Kenyon, S. J. 2015, *ApJ*, 812, 167
 Graham, M. J., Drake, A. J., Djorgovski, S. G., Mahabal, A. A., & Donalek, C. 2013, *MNRAS*, 434, 2629
 Graham, M. J., Kulkarni, S. R., Bellm, E. C., et al. 2019, *PASP*, 131, 078001
 Green, G. M., Schlafly, E., Zucker, C., Speagle, J. S., & Finkbeiner, D. 2019, *ApJ*, 887, 93
 Green, M. J., Hermes, J. J., Marsh, T. R., et al. 2018, *MNRAS*, 477, 5646
 Harding, L. K., Hallinan, G., Milburn, J., et al. 2016, *MNRAS*, 457, 3036
 Heber, U. 2016, *PASP*, 128, 082001
 Hermes, J. J., Gänsicke, B. T., Koester, D., et al. 2014, *MNRAS*, 444, 1674
 Hermes, J. J., Kilic, M., Brown, W. R., et al. 2012, *ApJL*, 757, L21
 Istrate, A. G., Marchant, P., Tauris, T. M., et al. 2016, *A&A*, 595, A35
 Kaplan, D. L., Bhalerao, V. B., van Kerkwijk, M. H., et al. 2013, *ApJ*, 765, 158
 Katz, M. L., Cooper, O. R., Coughlin, M. W., et al. 2020, arXiv:2006.06866
 Kilic, M., Brown, W. R., Allende Prieto, C., et al. 2011, *ApJ*, 727, 3
 Kilic, M., Brown, W. R., Allende Prieto, C., et al. 2012, *ApJ*, 751, 141
 Kilic, M., Brown, W. R., Gianninas, A., et al. 2014, *MNRAS*, 444, L1
 Koester, D., Dreizler, S., Weidemann, V., & Allard, N. F. 1998, *A&A*, 338, 612
 Kollmeier, J. A., Zasowski, G., Rix, H.-W., et al. 2017, arXiv:1711.03234
 Korol, V., Rossi, E. M., & Barausse, E. 2019, *MNRAS*, 483, 5518
 Korol, V., Rossi, E. M., Groot, P. J., et al. 2017, *MNRAS*, 470, 1894
 Kovács, G., Zucker, S., & Mazeh, T. 2002, *A&A*, 391, 369
 Kupfer, T., Bauer, E. B., Burdge, K. B., et al. 2019, *ApJL*, 878, L35
 Kupfer, T., Bauer, E. B., Burdge, K. B., et al. 2020a, arXiv:2007.05349
 Kupfer, T., Bauer, E. B., Marsh, T. R., et al. 2020b, *ApJ*, 891, 45
 Kupfer, T., Korol, V., Shah, S., et al. 2018, *MNRAS*, 480, 302
 Law, N. M., Kulkarni, S. R., Dekany, R. G., et al. 2009, *PASP*, 121, 1395
 Lomb, N. R. 1976, *Ap&SS*, 39, 447
 LSST Science Collaboration, Abell, P. A., Allison, J., et al. 2009, arXiv:0912.0201
 Marsh, T. R. 2001, in *Astromotography, Indirect Imaging Methods in Observational Astronomy*, ed. H. M. J. Boffin et al., Vol. 573 (Berlin: Springer), 1
 Marsh, T. R., Nelemans, G., & Steeghs, D. 2004, *MNRAS*, 350, 113
 Masci, F. J., Laher, R. R., Rusholme, B., et al. 2019, *PASP*, 131, 018003
 Merloni, A., Predehl, P., Becker, W., et al. 2012, arXiv:1209.3114
 Moore, C. J., Cole, R. H., & Berry, C. P. L. 2015, *CQGra*, 32, 015014
 Morris, S. L. 1985, *ApJ*, 295, 143
 Nelemans, G., Yungelson, L. R., & Portegies Zwart, S. F. 2001, *A&A*, 375, 890
 Nissanke, S., Vallisneri, M., Nelemans, G., & Prince, T. A. 2012, *ApJ*, 758, 131
 Oke, J. B., Cohen, J. G., Carr, M., et al. 1995, *PASP*, 107, 375

- Oke, J. B., & Gunn, J. E. 1982, *PASP*, 94, 586
- Patterson, J. 1994, *PASP*, 106, 209
- Perets, H. B., Zenati, Y., Toonen, S., & Bobrick, A. 2019, arXiv:1910.07532
- Perley, D. A. 2019, *PASP*, 131, 084503
- Pietrukowicz, P., Dziembowski, W. A., Latour, M., et al. 2017, *NatAs*, 1, 0166
- Piro, A. L. 2011, *ApJL*, 740, L53
- Postnov, K. A., & Yungelson, L. R. 2014, *LRR*, 17, 3
- Ramsay, G., Green, M. J., Marsh, T. R., et al. 2018, *A&A*, 620, A141
- Ramsay, G., Wheatley, P. J., Norton, A. J., Hakala, P., & Baskill, D. 2008, *MNRAS*, 387, 1157
- Reding, J. S., Hermes, J. J., Vanderbosch, Z., et al. 2020, arXiv:2003.10450
- Robson, T., Cornish, N. J., & Liu, C. 2019, *CQGra*, 36, 105011
- Roelofs, G. H. A., Rau, A., Marsh, T. R., et al. 2010, *ApJL*, 711, L138
- Scargle, J. D. 1982, *ApJ*, 263, 835
- Schwarzenberg-Czerny, A. 1996, *ApJL*, 460, L107
- Shen, K. J. 2015, *ApJL*, 805, L6
- Shen, K. J., Boubert, D., Gänsicke, B. T., et al. 2018a, *ApJ*, 865, 15
- Shen, K. J., Kasen, D., Miles, B. J., & Townsley, D. M. 2018b, *ApJ*, 854, 52
- Soares, E. D. A. 2017, arXiv:1701.02295
- Stroeer, A., Heber, U., Lisker, T., et al. 2007, *A&A*, 462, 269
- Taylor, J. H., & Weisberg, J. M. 1989, *ApJ*, 345, 434
- Thorne, K. S. 1987, *Three Hundred Years of Gravitation* (Cambridge: Cambridge Univ. Press), 330
- Tremblay, P. E., & Bergeron, P. 2009, *ApJ*, 696, 1755
- Tremblay, P. E., Bergeron, P., & Gianninas, A. 2011, *ApJ*, 730, 128
- Tremblay, P. E., Gianninas, A., Kilic, M., et al. 2015, *ApJ*, 809, 148
- Tulloch, S. M., & Dhillon, V. S. 2011, *MNRAS*, 411, 211
- Webbink, R. F. 1984, *ApJ*, 277, 355